Heliyon 10 (2024) e33644

Contents lists available at ScienceDirect

Heliyon

journal homepage: www.cell.com/heliyon

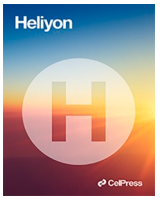

Research article

Efficient removal of sparfloxacin antibiotic from water using sulfonated graphene oxide: Kinetics, thermodynamics, and environmental implications

Chironjit Kumar Shaha [a,b], Md Abdullah Al Mahmud [c], Sudipta Saha [d], Subarna Karmaker [a], Tapan Kumar Saha [a,*]

[a] Department of Chemistry, Jahangirnagar University, Savar, Dhaka 1342, Bangladesh
[b] Veterinary Drug Residue Analysis Division, Institute of Food and Radiation Biology, Atomic Energy Research Establishment (AERE), Gonokbari, Savar, Dhaka 1349, Bangladesh
[c] Department of Chemistry, Louisiana State University, Baton Rouge, LA 70803, USA
[d] Department of Electrical and Electronic Engineering, Bangladesh University of Engineering and Technology, Dhaka 1205, Bangladesh

ARTICLE INFO

Keywords:
Sulfonated graphene oxide
Sparfloxacin
Adsorption
Kinetics
Equilibrium
Thermodynamics

ABSTRACT

Pharmaceutical contamination poses a significant threat to global health. Due to their high solubility in water, antibiotics are difficult to remove. This study produced and used sulfonated graphene oxide (SGO) to adsorb sparfloxacin from aquatic environments. UV–Visible, Fourier transform infrared (FTIR), X-ray diffraction (XRD), XPS, SEM, TEM, EDX, particle size, Thermogravimetric analysis (TGA), and acid-base titration were used to characterize synthesized SGO particles. The BET technique determined SGO's surface area (32.25 m^2/g). The calculated pH_{PZC} of SGO was 2.5. Sparfloxacin adsorption onto SGO was analyzed using adsorption duration, medium pH, adsorbent dosages, antibiotic concentration, cations, and solution temperature. The pseudo-second-order kinetic model better described experimental kinetic data than the pseudo-first-order and Elovich models. Equilibrium isotherm data supported the Langmuir model, revealing a peak absorption capacity of 1428.57 μmol/g at 25 °C. The kinetic and isotherm models' applicability was assessed using error analysis. A thermodynamic analysis revealed an endothermic, spontaneous adsorption process with a change in entropy (ΔS) of 114.15 J/mol K and enthalpy (ΔH) of 8.44 kJ/mol. A regeneration analysis showed that SGO adsorption efficiency topped 86.4 % after five cycles.

1. Introduction

The investigation of bioactive contaminants in aquatic environments has gained significant attention owing to the potential detrimental effects they may have on organisms. Antibiotics are a significant category of bioactive pollutants that infiltrate aquatic environments through various pathways, including hospital effluents [1], pharmaceutical waste [2], therapeutic drug disposal [3], and household waste [4]. Antibiotics are frequently detected in the following environments: surface water [5], groundwater [6], wastewater treatment plants [7], soils [8], vegetation [9], crops [10], and animal-derived foods (including meat, eggs, milk, and fish)

* Corresponding author.
E-mail address: tksaha_ju@yahoo.com (T.K. Saha).

https://doi.org/10.1016/j.heliyon.2024.e33644
Received 23 April 2024; Received in revised form 14 June 2024; Accepted 25 June 2024
Available online 25 June 2024

[11–14]. Antibiotic metabolites in aquatic environments have the potential to stimulate the development of antibiotic-resistant bacteria, thereby diminishing the efficacy of treatments against pathogens that affect humans and animals [15]. Consequently, it is essential to undertake the necessary measures to eliminate antibiotics from aquatic ecosystems.

The third largest class of antibiotics, fluoroquinolones, constituted 17 % of the antibiotic market in 2009 [16]. Approximately 70 % of consumed fluoroquinolones are excreted from the organism in an unmetabolized state, where they enter aquatic environments [17]. These substances exhibit solubility in aqueous solutions across a broad pH spectrum because they contain multiple acidic or basic functional groups (e.g., –COOH, $–NH_2$, and –OH) [18]. Sparfloxacin (Fig. 1), a prevalent broad-spectrum antibiotic belonging to the fluoroquinolone group, is utilized extensively for antibacterial purposes in aquaculture, poultry, and livestock [19]. Sparfloxacin molecules can persist for long periods in aquatic environments because of their stable structure [20]. A number of research studies have documented the adsorptive elimination of sparfloxacin from an aqueous solution utilizing the following adsorbents: sodium dodecyl sulfonate modified coordination polymer (CP/SDS) [21], calcium and cupric crosslinked alginate nanofibers (SA-Ca/Cu) [22], Fe_3O_4/graphene oxide/citrus peel-derived bio-char-based nanocomposite (mGOCP) [23], and magnetic graphene oxide (GO@Fe_3O_4) [24].

Activated carbon, carbon nanotubes, biochar, graphene, and graphene oxide, which are carbon-based adsorbents, have attracted significant attention due to their modifiable surface functionality, increased specific surface area, and extensive pore volume. These characteristics empower these materials to efficiently remove both organic and inorganic contaminants [25]. Graphene oxide (GO) is a two-dimensional material consisting of carbon atoms arranged in a honeycomb lattice and oxygen functional groups attached to its surface. GO exhibits high efficacy as an adsorbent for a wide range of contaminants, including antibiotics, owing to the multiplicity of molecular bonds supported by its oxygen-rich functional groups (carboxyl, epoxy, hydroxyl, sulfonate) [26]. Additionally, GO composites such as the FXM hydrogel (Fe(III)-tartaric acid/xanthan gum/graphene oxide/polyacrylamide), zinc oxide impregnated graphene oxide/inulin (ZGI), and Zn(II)-impregnated chitosan/graphene oxide composite (Zn(II)-CS/GO) have demonstrated considerable efficacy as adsorbents for the removal of a variety of fluoroquinolones, including levofloxacin, enrofloxacin, and ciprofloxacin, from aqueous solutions [27–29]. In recent years, sulfonated graphene oxide (SGO) has received considerable interest due to its exceptional catalytic efficiency and considerable adsorption capacity [30–32]. SGO surfaces with charged functional groups can interact electrostatically with oppositely charged molecules. SGO utilizes additional adsorption mechanisms, including hydrogen bonding and π-π stacking interactions, in order to capture aromatic pollutants [30]. The ability to regenerate and reuse SGO for numerous adsorption cycles makes it a financially viable and environmentally friendly substitute for antibiotic removal.

The objective of this study was to investigate the efficacy of SGO in the adsorptive removal of sparfloxacin from aqueous solution. SGO was synthesized with a minor modification to Tour's method [33]. It was characterized by using UV–Vis spectroscopy, Fourier transform infrared spectroscopy (FTIR), X-ray diffraction (XRD), X-ray photoelectron spectroscopy (XPS), Scanning electron microscopy (SEM), Transmission electron microscopy (TEM), Energy dispersive X-ray (EDX), Particle size, Thermogravimetric analysis (TGA), and acid-base titration techniques. The investigation of the adsorption behavior of sparfloxacin antibiotic onto SGO was conducted using principles of kinetics, equilibrium isotherm, and thermodynamics. An experimental investigation was undertaken to assess the impacts of different adsorption parameters, such as adsorption time, solution pH, adsorbent dose, sparfloxacin concentration, and temperature of the solution. The equilibrium adsorption of sparfloxacin onto SGO was observed at various temperatures. Several models were applied to analyze the kinetic data obtained from batch adsorption experiments; these models included pseudo-first-order, pseudo-second-order, Elovich, film diffusion, and intra-particle diffusion. The Langmuir, Dubinin-Radushkevich, Freundlich, and Temkin models were utilized to analyze the equilibrium adsorption isotherm data. Additionally, thermodynamic and activation parameters were assessed. Desorption, regeneration, and reuse performances of SGO as an adsorbent were evaluated to determine its economic viability.

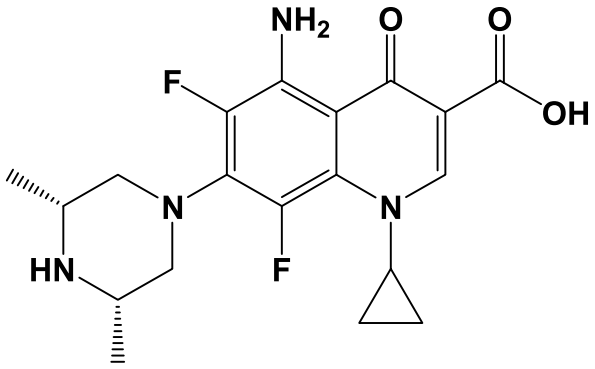

Fig. 1. Chemical structure of sparfloxacin.

2. Experimental

2.1. Chemicals

Exclusively substances of analytical grade were utilized in this investigation. Sparfloxacin and graphite flake were both obtained from Sigma-Aldrich and implemented in their original forms. A 5 mmol/L stock solution of sparfloxacin was formulated in dimethyl formamide (DMF). In order to produce working sparfloxacin solutions, they were diluted with water. The entire investigation was conducted using deionized water.

2.2. Sulfonated graphene oxide (SGO) synthesis

SGO was produced from graphite flake through a minor modification of the improved Hummers' method [33]. Following this, a solution consisting of 18.4 mol/L H_2SO_4 (360 mL) and 14.6 mol/L H_3PO_4 (40 mL) in a 9:1 (v/v) ratio was agitated for 30 min prior to the gradual addition of graphite particle (3.0 g). At 30 °C, solid $KMnO_4$ (18.0 g) was added to the solution gradually while agitating continuously with a magnetic stirrer. Following 24 h of stirring, 400 mL of cold water was poured over the resulting mixture. A volume of 3 mL of hydrogen peroxide (9.8 mol/L) was introduced into the mixture via dripping. The solid product was obtained through the spontaneous sedimentation method from the mixture. The acquired solid product was systematically deionized using 7.7 mol/L HCl, H_2O, ethanol, and ether. The solid product of SGO was desiccated in an oven at 60 °C for 12 h.

2.3. Characterization of SGO

The UV–Vis spectrum of SGO was obtained using a UV-1900i spectrophotometer manufactured by Shimadzu in Japan. The FTIR spectrum of SGO was measured in KBr at wavenumbers between 400 and 4000 cm^{-1} by utilizing a Shimadzu IRPrestige-21 FTIR Spectrophotometer. To ascertain the designated surface area, the BET (Brunauer, Emmett, and Teller) method was implemented.

Utilizing a Thermo Scientific™ ARL™ EQUINOX 1000 X-ray Diffractometer, the XRD spectra of graphite particle and SGO were acquired. At 30 mA, the CuK radiation source ($\lambda = 1.5418$ Å) was adjusted to 40 kV. The Debye-Scherrer equation (Eq. 1) was employed to ascertain the mean quantity of graphene sheets [34].

$$t = \frac{0.89\,\lambda}{\beta_{002} Cos\, \Theta_{002}} \tag{1}$$

$$n = \frac{1}{d_{002}} \tag{2}$$

In this context, t indicates the graphene layer thickness, θ represents the diffraction angle, β is the full width at half maximum (FWHM), d indicates the interlayer distance, and n indicates the number of layers.

A Scienta Omicron ESCA 2SR X-ray Photoelectron Spectroscope System, which was outfitted with a deluge source charge neutralizer, was employed to conduct the XPS measurements. For every analysis, a 300 W Mono Al K x-ray source (1486.6 eV) was employed, while the pressure within the analytical chamber was maintained at or below 5×10^{-9} mbar. As the calibration peak, C1s 284.8 eV was utilized in both high-resolution core level scans of each element and wide region survey scans. Utilizing the data processing software Casa XPS, the chemical state information was extracted from the deconvoluted core level spectra.

Utilizing an Oxford EDS/EBSD system integrated with a Thermo Fisher Helio G4 Xe plasma FIB/SEM system, SEM imaging and EDX analysis were conducted. The accelerating voltage utilized during the acquisition of SEM imaging and EDX data was 20 kV. In order to obtain the TEM imaging data, a 120 kV JEOL JEM-1400 TEM was operated using LaB6 filament.

Deionized water was employed as the dispersant in the moist dispersion method, which was utilized to examine the particle size distribution through the implementation of a particle size analyzer (Mastersizer 3000, Malvern Instruments Ltd., UK). TA instrument-Waters LLC was utilized to acquire TGA data in an inert atmosphere of nitrogen and air, supplemented with 2.16 mg of SGO at a heating rate of 10 °C/min. The data underwent analysis using the TRIOS 550 software.

2.4. Determination of pH_{PZC}

The determination of the point of zero charge (pH_{PZC}) of SGO was conducted using the pH drift method [35]. In a 125 mL stoppered vial, 50 mL of aqueous KCl solution (0.05 mol/L) were placed. To adjust the initial pH (pH_i) of the KCl solution from 2 to 12, a small amount of 0.1 mol/L HCl and NaOH was added. After adding 10 mg of SGO to each sample vial, the solution was allowed to equilibrate for a duration of 24 h. The final pH (pH_f) of the equilibrated solution was documented. The values of ΔpH were calculated by summing the variances of pH_i and pH_f. For the purpose of calculating pH_{PZC}, the ΔpH versus pHi graph was employed. The pH_{PZC} of SGO is calculated at the intersection of the experimental curve and the zero line.

2.5. Assessment of the surface functionality of SGO

In a 125 mL stoppered bottle, 50 mg of SGO was diffused in 50 mL of a reaction base (0.01 mol/L NaOH, 0.005 mol/L Na_2CO_3, or

0.01 mol/L $NaHCO_3$) and agitated for 48 h. The reaction bases that underwent SGO reaction were classified as post-reaction bases, whereas the bases that remained unreacted were classified as pre-reaction bases. Using methyl red as an indicator, aliquots (10 mL) of each reaction base were titrated with 0.01 mol/L HCl. The following equation (3) was utilized to ascertain the quantity of acidic functional groups per gram of SGO [31,36]:

$$n_{SF} = \frac{C_{HCl}\left(V_{HCl\_B,pre} - V_{HCl\_B,post}\right)}{m_{SGO}} \tag{3}$$

The concentration of the HCl titrant is denoted as C_{HCl}, while the volumes of the HCl for the pre-reaction and post-reaction bases are represented by $V_{HCl\_B,pre}$ and $V_{HCl\_B,post}$, respectively. The m_{SGO} represents the effective mass of SGO, while n_{SF} denotes the quantity of surface functionality. The n_{SF}, which is calculated using $NaHCO_3$, represents the combined number of sulfonic and carboxylic functional groups. Similarly, the n_{SF}, which is calculated using Na_2CO_3, represents the sum of sulfonic, carboxylic, and phenolic groups. Lastly, the n_{SF}, which is calculated using NaOH, represents the sum of sulfonic, carboxylic, lactonic, and phenolic groups. The determination of sulfonic group quantity was derived from EDX analysis of S content [37]. Carboxylic group quantity was ascertained by subtracting the concentration of sulfonic groups from the titration results utilizing $NaHCO_3$. Phenolic group quantity was ascertained by subtracting the concentrations of sulfonic and carboxylic groups from the titration results utilizing Na_2CO_3. Lastly, lactonic group quantity was ascertained by subtracting the concentrations of sulfonic, carboxylic, and phenolic groups from the titration outcomes utilizing NaOH.

2.6. Adsorption and desorption experiments

A batch adsorption procedure was carried out in a stoppered 125 mL vial containing 10 mg of SGO in 50 mL of 50 μmol/L aqueous sparfloxacin solution [38]. The pH of the sparfloxacin solution was adjusted to 5.5 using a digital pH meter (HACH, HQ11D) in conjunction with 0.1 mol/L HCl or NaOH solution. To reach equilibrium, the mixtures were stirred at 150 rotations per minute (rpm) for 240 min using a temperature-controlled mechanical shaker at room temperature (25 °C). To minimize water evaporation due to high temperatures, a lid was placed on each sample container. Samples were taken out at set intervals and then centrifuged at 9000 rpm for 1 min using a Flexpin Benchtop Centrifuge, LC 200, Japan, to separate the adsorbent material from the mixtures. The concentration of sparfloxacin in the supernatant was determined by spectrophotometric method at two specific wavelengths (λ_{max}: 298 nm, pH 2–6 and 290 nm, pH 7–11), utilizing a Shimadzu UV-1900i spectrophotometer (Shimadzu, Japan). It was determined that the molar absorptivity of sparfloxacin in aqueous solution is 28.0×10^3 L/mol.cm at 298 nm and 27.0×10^3 L/mol.cm at 290 nm. The amount of sparfloxacin adsorbed by SGO at time t, q_t (μmol/g), was determined by Equation (4) [38],

$$q_t = \frac{(C_0 - C_t)}{m} \times V \tag{4}$$

where C_0 (μmol/L) represents the initial concentration of sparfloxacin, C_t (μmol/L) denotes the concentration of sparfloxacin at time t, V (L) signifies the volume of solution, and m (g) implies the mass of SGO. The kinetics of sparfloxacin adsorption onto SGO were also investigated changing solution pHs (2−12), dosages of adsorbent (0.003−0.02 g), antibiotic concentrations (10−100 μmol/L), cations (Na^+, K^+, Mg^{2+}, and Ca^{2+}), and temperatures (25, 30, 35, and 40 °C), respectively.

Additionally, the equilibrium adsorption of sparfloxacin onto SGO was conducted at various temperatures (25, 30, 35, and 40 °C) in aqueous solution at pH 5.5. At equilibrium time, the sparfloxacin adsorption per gram of SGO, q_e (μmol/g), and % removal of sparfloxacin were calculated as follows [38]:

$$q_e = \frac{(C_0 - C_e)}{m} \times V \tag{5}$$

$$\text{Sparfloxacin removal } (\%) = \frac{(C_0 - C_e)}{C_0} \times 100 \tag{6}$$

here C_e (μmol/L) represents the equilibrium concentration of sparfloxacin; C_0, V, and m have the same meaning as previously stated.

A study on desorption and regeneration of SGO was conducted in order to assess its economic viability. Desorption of sparfloxacin from sparfloxacin-loaded SGO was investigated in a 1 mol/L HCl in DMF solution. To begin, sparfloxacin was introduced onto SGO under ideal adsorption conditions. By employing centrifugation at 9000 rpm, the sparfloxacin-loaded SGO was isolated from the adsorption medium and subsequently washed with deionized water. Following thorough drying in an oven set at 60 °C, the sample was utilized in the desorption experiment. A solution containing 50 mL of acidic DMF was mixed with 10 mg of sparfloxacin-loaded SGO and stirred with a mechanical agitator until equilibrium desorption was achieved. The concentration of desorbed sparfloxacin in the acidic DMF solution was then measured using a UV–Vis spectrophotometer. Deionized water was used to completely purify regenerated SGO until the pH was neutral. Following the regeneration process, the adsorbent was desiccated at 100 °C, weighed, and reused in the subsequent adsorption experiment. The SGO underwent a maximum of five cycles of regeneration. All empirical data presented in this manuscript is calculated as the mean of two evaluations.

2.7. Error analysis

The statistical technique root-mean-square error (RMSE) is commonly used to evaluate the difference between predicted values from a model (both kinetic and isotherm) and the actual experimental values [39]. In this study, the appropriateness of the kinetic and isotherm models was assessed using the following Equation (7):

$$\mathrm{RMSE} = \sqrt{\frac{1}{N-p}\sum_{i=1}^{N}\left(q_{exp-}\, q_{cal}\right)^2} \tag{7}$$

The experimental response values are represented as q_{exp}, while the model-predicted response values are denoted as q_{cal}. The quantity of experimental runs is denoted as N, while the parameter of kinetic or isotherm models is p.

3. Results and discussion

3.1. Synthesis and characterization of SGO

SGO was synthesized using the modified Hummers' method described by Marcano et al. [33], with minor adjustments as outlined earlier. Various analytical techniques, including UV–Vis spectroscopy, Fourier transform infrared spectroscopy (FTIR), surface area analysis, X-ray diffraction (XRD), X-ray photoelectron spectroscopy (XPS), scanning electron microscopy (SEM), transmission electron microscopy (TEM), energy dispersive X-ray (EDX), particle size analysis, thermogravimetric analysis (TGA), and acid-base titration, were employed to characterize the newly synthesized SGO.

3.2. UV–Vis spectrum analysis

The UV–Vis spectrum of SGO (0.1 g/L) in an aqueous solution is depicted in Fig. 2a. SGO exhibits a prominent peak at 231 nm,

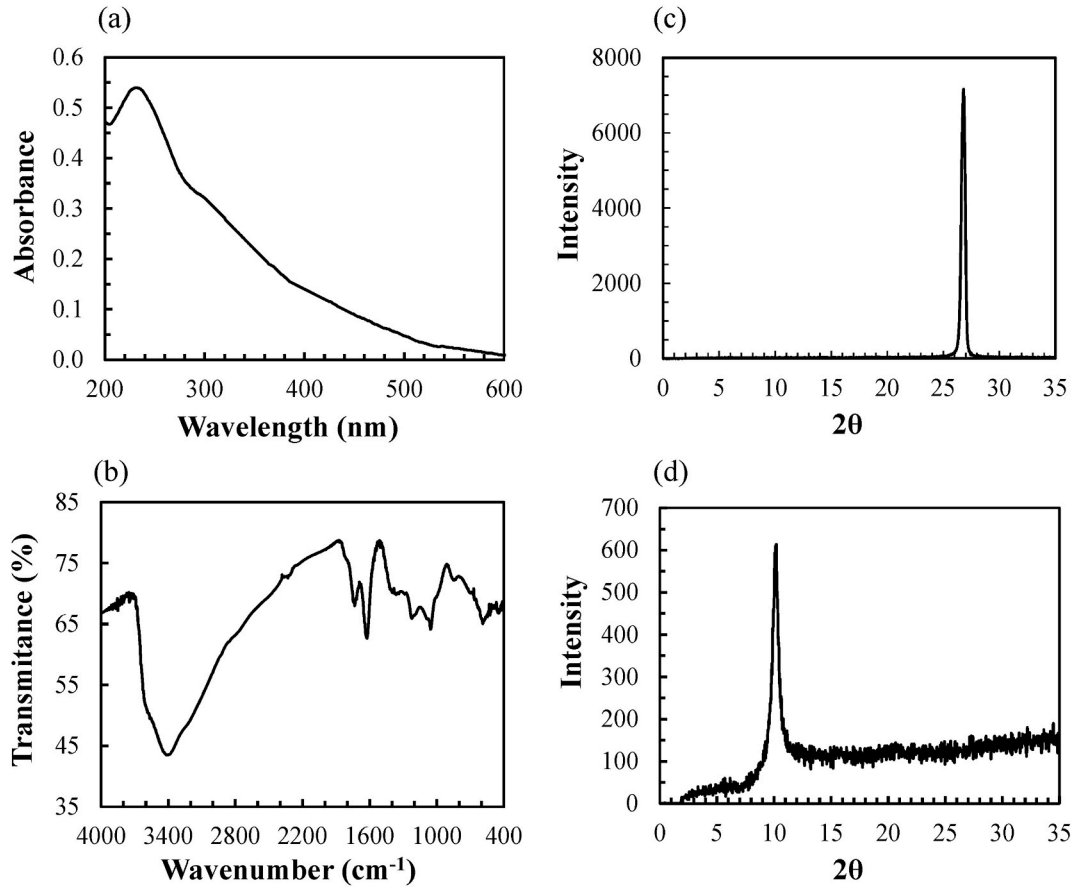

Fig. 2. Typical UV–Vis spectrum of SGO (0.1 g/L) in aqueous medium (a); FTIR spectrum of SGO recorded in KBr (b); XRD spectra of graphite (c); and SGO (d).

attributed to the π to π* transitions of aromatic conjugated –C=C– bonds, as indicated by its absorbance spectrum. At 300 nm, the weak absorption (shoulder) is a result of the n to π* transitions of carboxylic carbonyl and hydroxyl auxochromes [40]. These results indicate that there are oxygen functional groups conjugated to aromatic domains on SGO [41,42]. From Fig. S1, it is noted that the direct band gap of SGO was found to be 3.74 eV which is pretty much close to the direct band gap of GO reported by Gupta et al. [43].

3.3. FTIR spectrum analysis

Fig. 2b illustrates the FTIR spectrum of SGO. The wide and strong peak noted at around 3406 cm^{-1} can be ascribed to the stretching vibration of the O–H bond present in SGO. The O–H band is generated by intercalated H_2O, sulfonic acid O–H, carboxylic acid O–H, which is directly bonded to SGO [44–46]. Peak observed at 1734 cm^{-1} is attributable to the carboxylic C=O group. The pronounced peak observed at 1624 cm^{-1} can be attributed to the stretching and bending vibrations of O–H that occur within intercalated H_2O molecules [41]. The peaks observed at 1053 cm^{-1}, 1221 cm^{-1}, and 1361 cm^{-1} are due to the stretching vibrations of C–O, C–O–C, and C–OH, respectively [41]. The peaks observed at 1082 cm^{-1} and 1287 cm^{-1} are a result of the symmetric and asymmetric vibrations of the O=S=O group [46–48]. The band observed at 840 cm^{-1} corresponds to the stretching vibration of S–O bond of the sulfonic acid groups in SGO [47].

3.4. XRD examination

Fig. 2 illustrates the diffractograms of graphite and SGO. The distinct diffraction peak of graphite is seen at an angle of $2\theta = 26.8^{\circ}$ (Fig. 2c), indicating the presence of the (002) plane in the hexagonal graphite structure, with a layer spacing of 0.33 nm. The diffraction peak detected at an angle of 10.3° (2θ) corresponds to the reflection of the (001) plane in the hexagonal crystal structure of SGO, as shown in Fig. 2d. The distance between consecutive carbon basal planes, known as the d-spacing, is 0.86 nm [49–51]. A greater distance between adjacent carbon basal planes indicates the presence of H_2O and oxygen-containing functional groups within the carbon layer structure. It was determined that the mean number of graphene layers for SGO was 8, while the mean layers number for graphite was 61. Moreira et al. have reported similar findings for GO [34].

3.5. XPS examination

An XPS examination was performed to examine the valence states and elemental compositions of the SGO. Fig. 3 displays the high-resolution wide range XPS spectra of SGO. The survey spectrum of SGO in Fig. 3a clearly shows a dominant C1s peak at about 284 eV, a

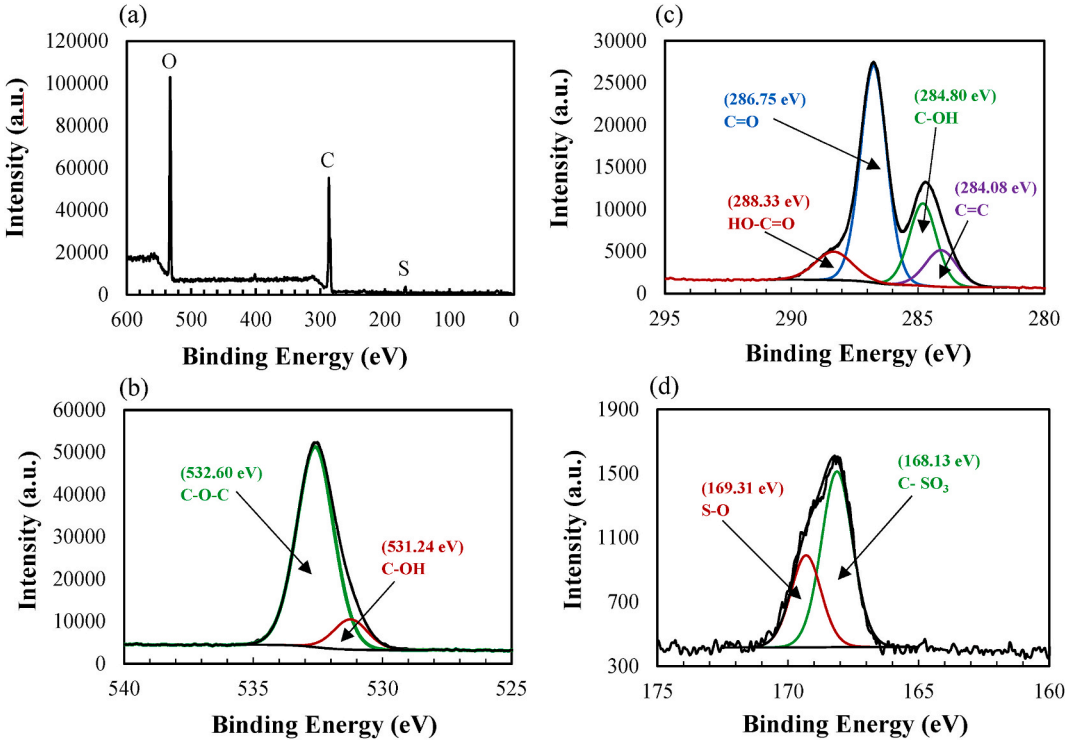

Fig. 3. (a) The broad scan XPS spectrum of SGO; Spectra of C1s (b) and O1s (c) at the core level with high resolution; and (d) Spectra of S2p at the core level with high resolution.

prominent O1s peak at approximately 532 eV, and a very faint S2p peak at around 168 eV. The high resolution spectra at the C1s level comprise four components, each of which corresponds to a distinct carbon functional group. The energy bands located at 284.08 eV, 284.80 eV, 286.75 eV, and 288.33 eV correspond to carbon atoms in the functional groups C=C (atom% 11.37), C–OH (atom% 22.06), C=O (atom% 56.22), and HO–C=O (atom% 10.35) accordingly (Fig. 3b). Similarly, the high-resolution spectra of O1s reveal two O components: C–OH (atom% 12.19) at 531.24 eV and C–O–C (atom% 87.81) at 532.60 eV (Fig. 3c) [52]. The existence of sulfonic acid groups on SGO is verified by the distinct peaks (S2p) at 168.13 eV and 169.31 eV for S–O (atom% 50.01) and S–C (atom% 49.99), respectively [46,53,54].

3.6. Surface morphology

The scanning electron microscopy (SEM) image of SGO (Fig. 4a) reveals that the SGO sheets have distinct edges and wrinkled textures and are arbitrarily aggregated. The SEM has detected SGO sheets with lateral dimensions of up to 40 μm and particles measuring a few microns in the same SGO samples [55]. The TEM image of SGO (Fig. 4b) displays a characteristic folded and wrinkled morphology, consisting of single or extremely thin layers (higher transparency areas denote these layers), whereas dark patches represent thick films composed of numerous SGO layers [56].

3.7. Composition and distributions of acidity

Utilizing energy dispersive X-ray (EDX), the elemental composition of SGO was quantified. Carbon, oxygen, sulfur, and other element peaks corresponding to their respective binding energies are displayed in Fig. 4c of the EDX spectrum. Along with the primary constituents C (56.41 %), O (40.38 %), and S (2.24 %), SGO also comprises impurities (0.97 %). From the basic materials, these minute quantities of impurities may pass. SGO exhibited the greatest interlayer distance and a significant degree of oxidation, as indicated by its C/O ratio of 1.86 [57]. According to Basak et al., SGO is predominantly composed of C (50.41 %), O (46.47 %), and S (3.12 %) [37].

Acid-base titration was utilized to ascertain the surface acidic functional groups of SGO [31,36]. Carboxylic groups (1.38 mmol/g) were found to be the most abundant on the SGO surface, surpassing phenolic (0.71 mmol/g), sulfonic (0.72 mmol/g), and lactonic

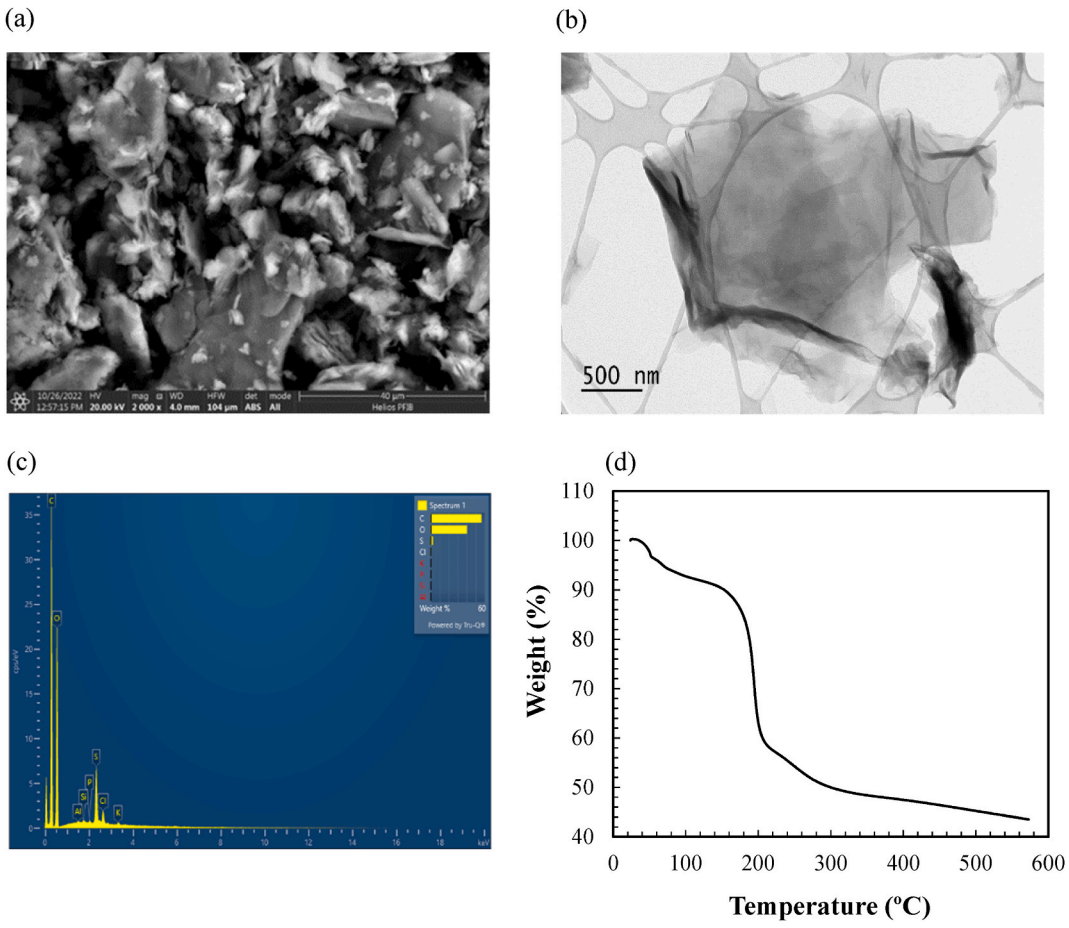

Fig. 4. (a) SEM image of SGO; (b) TEM image of SGO; (c) EDX analysis of SGO; and (d) Thermogravimetric analysis of SGO.

groups (0.70 mmol/g). The total quantity of acidic groups on the SGO surface was approximated to be 3.9 mmol/g. Hou et al. [31] reported values of 0.63 mmol/g for carboxylic groups, 0.75 mmol/g for phenolic groups, 0.8 mmol/g for sulfonic groups, and 0.24 mmol/g for lactonic groups in SGO, which are comparable to the observed results.

3.8. Thermogravimetric examination

As illustrated in Fig. 4d–a thermogravimetric analysis (TGA) was performed to assess the thermal stability of SGO. The Thermogravimetric analysis (TGA) plot indicates a 10 % mass loss in SGO at temperatures below 150 °C, which may be ascribed to water that has been adsorbed and intercalated [58]. A 32 % mass loss between 150 and 200 °C is attributed to oxygen-containing functional groups, including CO, CO_2, and others [47]. A further reduction in mass loss beyond 200 °C is ascribed to the sulfonic acid groups liberated from the surface of the SGO [58].

3.9. Size of particles analysis

As determined by laser diffraction, the size distribution of SGO particles is illustrated in Fig. 5a. A diverse range of particle diameters, between 0.87 μm and 110 μm, were identified. 10 % of the particles maintained a diameter of less than 4.61 μm, while 50 % maintained a diameter of less than 22.3 μm. On the contrary, 90 % of the SGO particles had a size of less than 68.5 μm. There were considerably fewer particulates exceeding 100 μm in size.

3.10. Area of surface analysis

The N_2 adsorption–desorption isotherm for SGO is depicted in Fig. 5b. The presence of an H3 hysteresis loop in the relative pressure

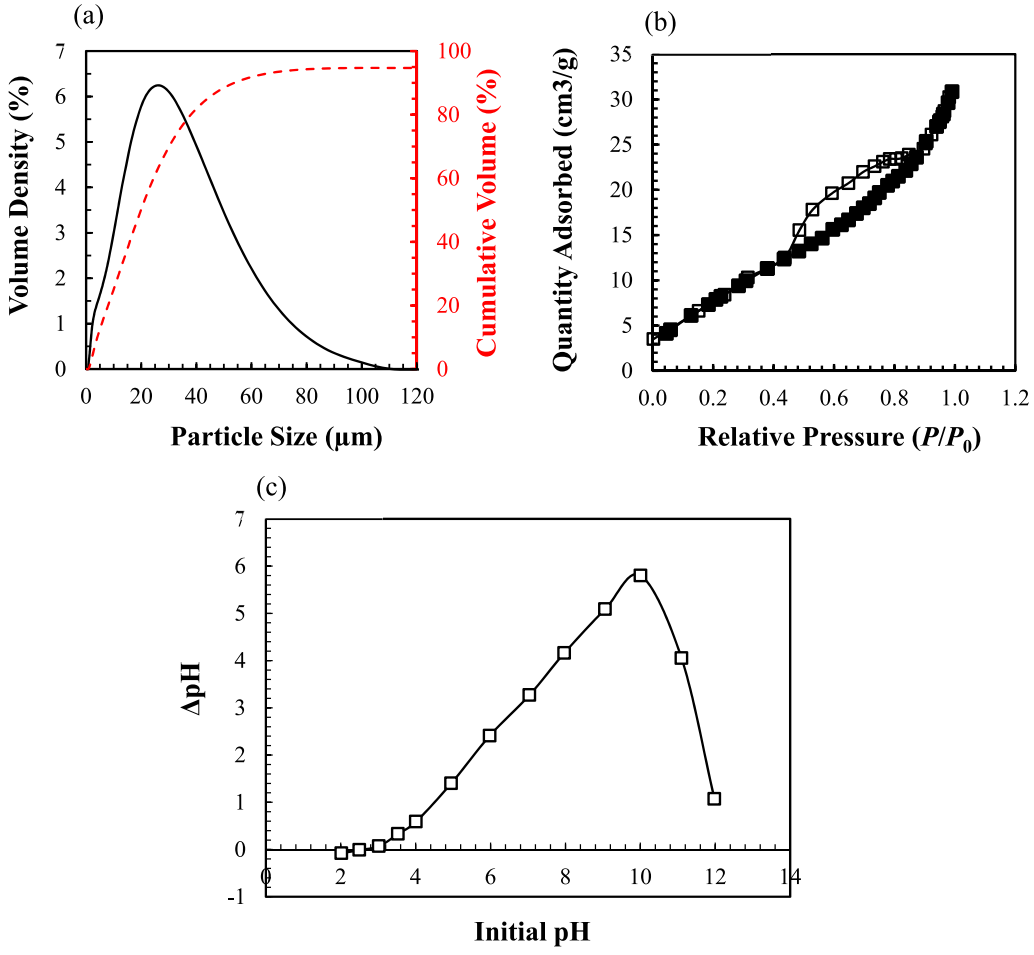

Fig. 5. (a) The particle size distribution pattern of SGO as determined by laser diffraction technique; (b) The isotherm of N_2 adsorption−desorption for SGO; and (c) The measurement of the point of zero charge (pH_{PZC}) of SGO.

range (P/P_0) of 0.44–0.90 in the type IV isotherm curve indicates the porous nature of the substance [59], as depicted in the TEM image of SGO in Fig. 4b. The specific surface area of the SGO sample was measured to be 32.25 m^2/g using the BET method. The primary reason for the relatively small surface area of SGO compared to activated carbon [60] was identified as the severe agglomeration of SGO sheets during the drying process [59]. In contrast, the BET surface area value of GO was 20.93 m^2/g [59], indicating a comparatively low value. This implies that the synthesized SGO has significant potential as an adsorbent material.

3.11. Point of zero charge (pH_{PZC}) of SGO

The term "point of zero charge" (pH_{PZC}) describes the condition in which a surface does not have any electrical charge density. The pH drift method was used to determine the pH_{PZC} value of SGO [35]. The pH_{PZC} value for SGO was estimated to be 2.5 based on the relationship between ΔpH and initial pH, as depicted in Fig. 5c. Based on this result, the surfaces of SGO will function as positively charged surfaces for pH values below 2.5 and negatively charged surfaces for pH values above 2.5. Conversely, Oluwasina et al. documented that SGO possesses a pH_{PZC} value of 4.6 [61].

4. Implications of contact time

An experiment was conducted to examine the impact of contact duration on the adsorption of 50 μmol/L sparfloxacin onto SGO in an aqueous solution with a pH of 5.5, at a temperature of 25 °C. The variations in contact time are depicted in Fig. 6. Fig. 6a shows the time-dependent UV–visible absorption spectra of sparfloxacin during the adsorption onto SGO in an aqueous medium. As the interaction time increased, the absorbance of sparfloxacin at 298 nm consistently reduced, as depicted in Fig. 6a. Fig. 6b depicts the correlation between q_t and contact time, t. The adsorption of sparfloxacin onto SGO was shown to have a fast initial phase of 15 min, followed by a slower phase with a reduced rate. Equilibrium was achieved within 60 min. The initial quick adsorption can be ascribed to the electrostatic interaction between sparfloxacin and SGO [38,62]. Nevertheless, as the surface of SGO reached its maximum capacity with sparfloxacin, the rate at which sparfloxacin molecules were being adsorbed gradually decreased, and they started to penetrate into the pores of SGO. There was no significant increase in the amount of antibiotic adsorption with time after reaching equilibrium at around 240 min. An analogous outcome was noted when cefixime was adsorbed onto chitosan in an aqueous solution [38]. For the subsequent investigations, an interaction period of 240 min was established in order to achieve absolute adsorption equilibrium.

4.1. Implications of solution pH

The pH of the solution greatly affects the adsorption of sparfloxacin onto SGO. This is because the pH regulates the ionization states of sparfloxacin molecules and the surface charge of SGO in water. The pH_{PZC} value of SGO was found to be 2.5, indicating that its surface exhibited a negative charge at pH levels higher than 2.5. Sparfloxacin exhibits two distinct acid dissociation constants (pK_{a1} = 6.3 and pK_{a2} = 8.8) and can exist in a cationic (pH < pK_{a1}), anionic (pH > pK_{a2}), or neutral state (pK_{a1} < pH < pK_{a2}) configuration, depending on the solution pH (Fig. 7) [23]. Consequently, the ionization states of sparfloxacin and SGO in aqueous solution are

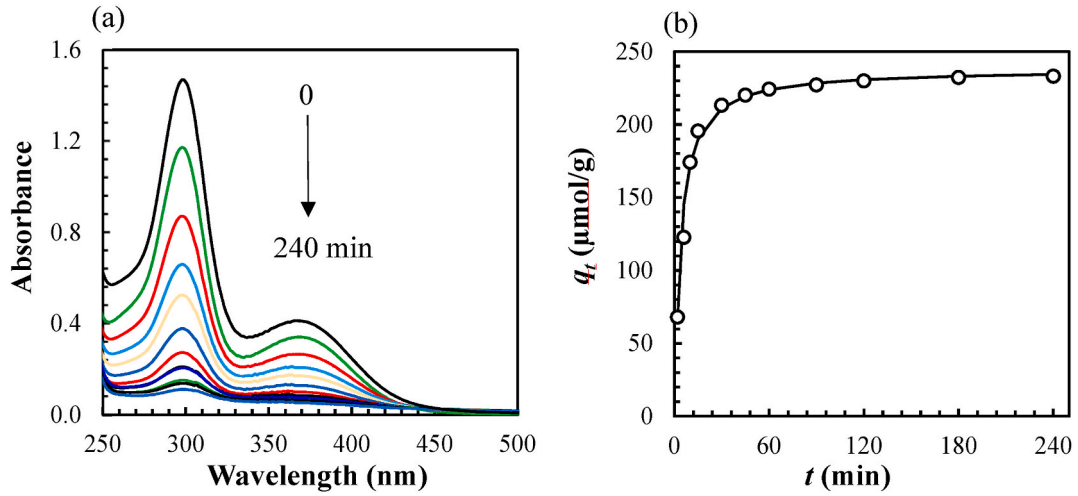

Fig. 6. (a) Typical changes in UV–visible absorption spectra of sparfloxacin at various time intervals during adsorption onto SGO in aqueous solution at 25 °C. The spectra were taken at 0, 2, 6, 10, 15, 30, 45, 60, 90, 120, 180, and 240 min, respectively ($[Sparfloxacin]_0$: 50 μmol/L; solution volume: 0.05 L; pH 5.5; SGO: 0.01 g). (b) The variations in the adsorption capacity (q_t) of sparfloxacin onto SGO as a function of contact time, t, in aqueous solution at 25 °C. The solid line represents the adsorption kinetic traces modeled using the pseudo-second-order equation (Eq. 9) and the corresponding $q_{e(cal)}$ and k_2 values found in Table 1.

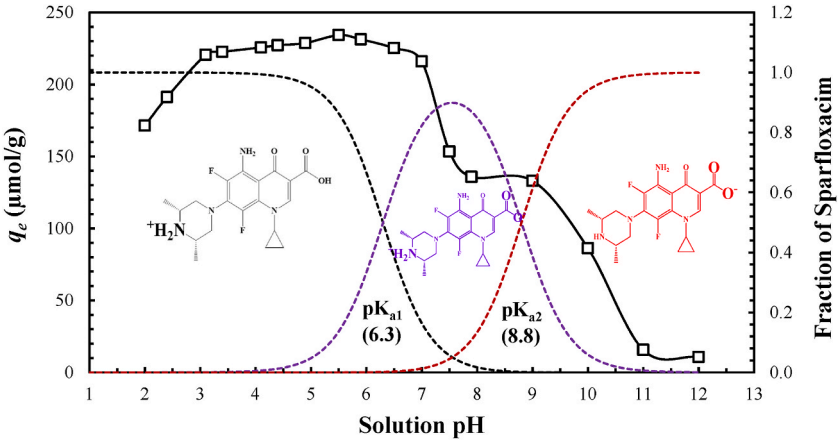

Fig. 7. The impact of solution pH on sparfloxacin uptake onto SGO in aqueous solutions. ([Sparfloxacin]$_0$: 50 µmol/L; Solution volume: 0.05 L; SGO: 0.010 g; pH: 2–12; temperature: 25 °C).

significantly pH dependent. Fig. 7 demonstrates the impact of solution pH, which varies from 2 to 12, on the adsorption of sparfloxacin with SGO. It was observed that the q_e value increased as the solution's pH rose from 2 to 3.1, remained nearly constant until pH 7, and then decreased considerably at pH > 7. The maximal adsorption capacity of sparfloxacin onto SGO was determined to be 234.22 µmol/g at a solution pH of 5.5. The observed low q_e values between pH 2 and 2.4 can potentially be ascribed to an electrostatic repulsion between the protonated sparfloxacin molecules (pH < pK$_{a1}$) and the positively charged SGO surface (pH < pH$_{PZC}$). Furthermore, it is worth noting that sparfloxacin molecules may face competition for surface binding sites on the SGO due to the presence of a significant number of H^+ ions in a highly acidic solution. This competition could potentially restrict the q_e value of the SGO [23]. The reduction in q_e value at higher pH levels can be ascribed to both the repulsion between deprotonated sparfloxacin molecules (pH > pK$_{a2}$) and the negatively charged SGO surface (pH > pH$_{PZC}$) and the competition between OH^- ions and deprotonated sparfloxacin molecules for surface binding sites on the SGO. Comparable results were also noted when sparfloxacin was adsorbed onto mGOCP [23] and cefixime was adsorbed onto chitosan [38] in aqueous solutions. Therefore, the subsequent investigations were conducted in aqueous solution at pH 5.5.

4.2. *The impact of dosage*

A study was conducted to determine the influence of the amount of adsorbent on the adsorption of sparfloxacin using SGO at various dosage levels ranging from 3 to 20 mg. Fig. 8 illustrates that when the dosage of SGO increased, the percentage of sparfloxacin adsorption increased from 65.8 % to 96.5 %. In contrast, the volume (0.05 L) and concentration of the sparfloxacin solution (50 µmol/L) remained unchanged. This is a result of the enlargement of accessible adsorption sites and the concomitant augmentation in surface areas of SGO. In contrast, there was a significant decrease in the amount of sparfloxacin absorbed per gram of adsorbent (q_e) from 538.7 to 118.6 µmol/g as the mass of SGO increased (Fig. 8). Mathematically speaking, this result can be explained by combining equations (5) and (6). Equation (5) demonstrates an inverse relationship between the quantity of sparfloxacin absorption (q_e) and the mass of adsorbent (m). Increasing the mass of the adsorbent leads to a decrease in the values of q_e for a fixed percentage of antibiotic

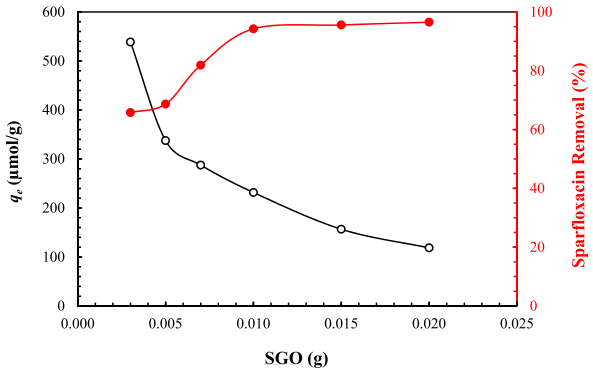

Fig. 8. The alterations in the equilibrium adsorption capacity (q_e) and removal percentage (%) of sparfloxacin onto SGO were investigated using various dosages of SGO in an aqueous medium ([Sparfloxacin]$_0$: 50 µmol/L; solution volume: 0.05 L; SGO: 0.003–0.020 g, pH: 5.5, temperature: 25 °C).

adsorption, as the volume (V) and initial concentrations of sparfloxacin (C_0) stay unchanged. Analogue results were also noted when sawdust treated with hexadecylpyridinium bromide and the marine alga P. *yezoensis* Ueda were utilized to extract the dyes allura red AC [63] and Congo red [64] from aqueous solutions, respectively.

4.3. Effects of concentration of sparfloxacin

To study the rate at which sparfloxacin is adsorbed, we measured the amount of sparfloxacin adsorbed onto SGO by changing the concentration of the antibiotic in the solution from 10 to 100 μmol/L. This was done at a pH of 5.5, with a fixed amount of SGO (0.01 g), and at a temperature of 25 °C. Fig. 9 depicts the correlation between the adsorption of sparfloxacin onto SGO (q_t, μmol/g) and the interaction time (t, min) at various doses of sparfloxacin. As the concentration of sparfloxacin rose, both the initial rate (h, μmol/g min) and the amount of antibiotic adsorption onto SGO (q_e, μmol/g) increased (Table 1). As the antibiotic concentration grew from 10 to 100 μmol/L, the corresponding values of q_e increased from 45.54 to 371.96 μmol/g (Fig. 9). The results suggest that the initial concentration of the antibiotic in the solution is crucial for driving the adsorption process, effectively overcoming any barriers to the mass transfer between the adsorbate and the adsorbent [65]. Analogous results were also observed when cefixime [38], remazol brilliant violet (RBV) [66], and reactive black 5 (RB5) [67] were extracted from aqueous solution using chitosan.

4.4. The impact of salts

To investigate the influence of inorganic salts on the adsorption process, a variety of salts were added to sparfloxacin solution. The impact of salts was assessed by systematically introducing 0.1 mol/L of Na_2SO_4, K_2SO_4, $CaSO_4$, and $MgSO_4$ into the adsorption medium. In Fig. 10, the antibiotic absorption capacity of SGO in aqueous solution (pH 5.5) containing added salts at 25 °C is illustrated. Sparfloxacin adsorption onto SGO in aqueous solution is inhibited by all metal ions in the following order: $Ca^{2+} > Mg^{2+} > K^+ > Na^+$. The aforementioned phenomenon can be ascribed to the aggregation of SGO induced by the presence of inorganic ions in the solution. The current sequence of sparfloxacin adsorption onto SGO is consistent with the order in which SGO aggregates in aqueous solution due to metal ions is reportedly as follows: $Ca^{2+} > Mg^{2+} > K^+ > Na^+$ [68]. Due to the considerable impact of ions on the adsorption process, sparfloxacin may be adsorbed onto SGO through a mechanism that involves electrostatic outer sphere adsorption.

4.5. The implications of temperature

At different temperatures, sparfloxacin adsorption onto SGO was observed in an aqueous medium (pH 5.5) while holding all other experimental parameters constant. In Fig. 11, the impacts of temperature are illustrated. As indicated in Table 1, the initial uptake rate (h) of sparfloxacin increased significantly from 72.46 to 126.58 μmol/g min as the solution temperature rose from 25 °C to 40 °C. This may be attributed to the fact that elevated temperatures increase the dispersibility of SGO in aqueous solutions. It is observed that as the temperature rose from 25 °C to 40 °C, the equilibrium absorption capacity (q_e) of sparfloxacin marginally increased from 231.25 to 233.21 μmol/g. This phenomenon could be attributed to an increase in the quantity of active binding sites present on the surface of the SGO or in the diffusion rate of sparfloxacin [69]. It has been established that as the temperature of the solution rises, the rate at which adsorbate molecules spread across the surface layer and penetrate the inner cavities of the adsorbent also increases. Comparable results were also noted when sawdust and sawdust treated with hexadecylpyridinium bromide were employed to extract Allura Red AC from an aqueous solution, respectively [63].

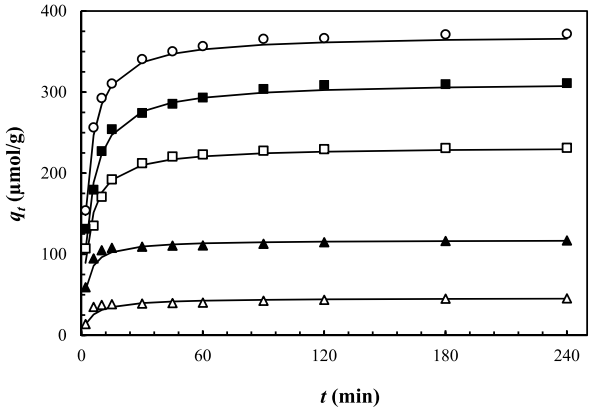

Fig. 9. The relationship between adsorption capacity (q_t) of sparfloxacin onto SGO and contact time (t) at various concentrations of sparfloxacin in aqueous solution. (Solution volume: 0.05 L; SGO: 0.010 g; temperature: 25 °C; pH: 5.5; $[Sparfloxacin]_0$: Δ: 10 μmol/L; ▲: 25 μmol/L; □: 50 μmol/L; ■: 75 μmol/L; ○: 100 μmol/L). Equation (9) was utilized to numerically simulate each line, with the values of $q_{e(cal)}$ and k_2 being provided in Table 1.

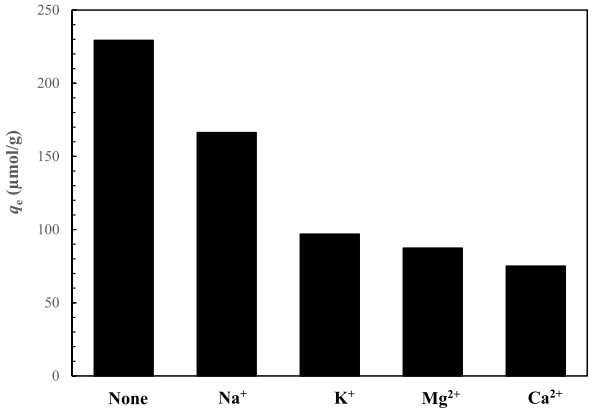

Fig. 10. Variations in the equilibrium adsorption capacity (q_e) of sparfloxacin onto SGO in an aqueous solution containing different inorganic ions. ([Sparfloxacin]$_0$: 50 μmol/L, solution volume: 0.05 L, SGO: 0.010 g, pH: 5.5, temperature: 25 °C).

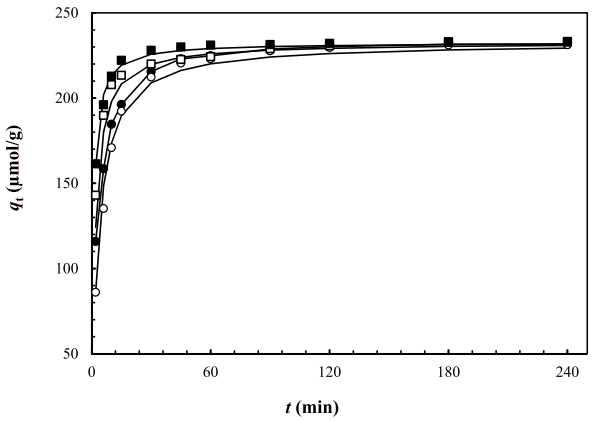

Fig. 11. The variation in the adsorption capacity of sparfloxacin (q_t) onto SGO with contact time (t) in aqueous solution (pH 5.5) at distinct temperature conditions ([Sparfloxacin]$_0$: 50 μmol/L; solution volume: 0.05 L; SGO: 0.010 g; Temperature: ○: 25 °C; ●: 30 °C; □: 35 °C; and ■: 40 °C, respectively). Equation (9) was employed to simulate each line, with the $q_{e(cal)}$ and k_2 values listed in Table 1.

4.6. Kinetic simulation

Utilizing the pseudo-first-order [70], pseudo-second-order [71], Elovich [72], film diffusion [73], and intraparticle diffusion [74] kinetic models, the kinetics and mechanisms of sparfloxacin adsorption onto SGO were analyzed, respectively. The pseudo-first-order kinetic model can be represented by the following linear equation:

$$\log (q_e - q_t) = \log q_e - \frac{k_1}{2.0303} t \tag{7}$$

where k_1 (1/min) represents the adsorption rate constant in the pseudo-first-order kinetic model. In order to determine the value of k_1, the slope of a linear plot $\log(q_e - q_t)$ versus t was computed.

The following equations characterize the linear and nonlinear variations of the pseudo-second-order kinetic model:

$$\frac{t}{q_t} = \frac{1}{k_2 q_e^2} + \frac{1}{q_e} t \tag{8}$$

$$q_t = \frac{k_2 q_e^2 t}{(1 + k_2 q_e t)} \tag{9}$$

where k_2 (g/μmol min) represents the adsorption rate constant in the pseudo-second-order kinetic model. The values of k_2 and q_e were estimated using the intercept and slope of a plot t/q_t versus t. The subsequent equation is employed to determine the initial rate, denoted as h (μmol/g min), of sparfloxacin adsorption:

Table 1
Summary of kinetic parameters of adsorption process at various sparfloxacine concentrations and solution temperatures.

Parameters	[Sparfloxacine]$_0$ (μmol/L)					Temperature (°C)			
	10	25	50	75	100	25	30	35	40
$q_{e(exp)}$ (μmol/g)	45.54	116.96	231.25	311.07	371.96	231.25	231.79	232.86	233.21
Pseudo-First-Order Kinetic Model									
$k_1 \times 10^{-3}$ (1/min)	19.40	20.30	34.50	28.0	28.60	34.50	33.40	31.70	32.60
$q_{e(cal)}$ (μmol/g)	14.17	20.93	80.02	108.79	109.80	80.02	65.87	61.43	24.31
R^2	0.904	0.873	0.975	0.952	0.953	0.975	0.969	0.958	0.959
RMSE	34.40	104.45	162.49	217.17	282.88	162.49	179.03	186.06	217.0
Pseudo-Second-Order Kinetic Model									
$k_2 \times 10^{-3}$ (g/μmol min)	4.52	3.82	1.34	0.81	0.90	1.34	1.71	1.85	2.34
h (μmol/g min)	9.60	52.91	72.46	78.74	123.46	72.46	92.59	100.0	126.58
$q_{e\ (cal)}$ (μmol/g)	46.08	117.65	232.56	312.5	370.37	232.56	232.56	232.56	232.56
R^2	0.999	1.0	1.0	1.0	1.0	1.0	1.0	1.0	1.0
RMSE	4.11	4.86	8.59	10.24	6.66	8.59	5.10	5.88	4.80
Elovich Kinetic Model									
$\alpha \times 10^3$ (μmol/g min)	0.31	22.72	1.26	1.14	2.96	1.26	4.22	8.62	25.40
$\beta \times 10^{-3}$ (g/μmol)	199.76	107.50	37.19	26.46	24.24	37.19	42.80	46.01	50.76
R^2	0.749	0.725	0.895	0.917	0.867	0.895	0.886	0.861	0.843
RMSE	4.61	9.11	14.67	18.03	25.71	76.73	66.58	62.16	56.48
Activation Parameters									
E_a (kJ/mol)						27.16			
R^2						0.968			
$\Delta G^{\ddagger}$ (kJ/mol)						55.62	56.13	56.64	57.15
$\Delta H^{\ddagger}$ (kJ/mol)						24.62			
$\Delta S^{\ddagger}$ (J/mol K)					−102.29				
R^2						0.961			

$$h = k_2 q_e^2 \tag{10}$$

The Elovich kinetic model is represented as follows:

$$q_t = \frac{1}{\beta}\ln(\alpha\beta) + \frac{1}{\beta}\ln t \tag{11}$$

In this context, α (μmol/g min) represents the initial rate at which antibiotics are adsorbed, while β (g/μmol) denotes the surface coverage and sorption activation energy, respectively. By analyzing the relationship between q_t and ln$t$, the magnitudes of α and β were estimated.

Table 1 contains the values of the adsorption parameters derived from the fitted kinetic models. In contrast to the pseudo-second-order kinetic model, which produced R^2 values of ≥0.999, the pseudo-first-order and Elovich kinetic models were unable to generate statistically significant R^2 values (≤0.975 and ≤ 0.917, respectively). The experimental $q_{e(exp)}$ values and the calculated $q_{e(cal)}$ values derived from the pseudo-second-order kinetic model agreed exceptionally well (Table 1). Moreover, the pseudo-second-order kinetic model demonstrated lower RMSE values (4.11–10.24) compared to the pseudo-first-order (34.40–282.88) and Elovich models (4.61–76.73). The kinetic mechanism of sparfloxacin adsorption onto SGO is consistent with the pseudo-second-order kinetic model, as demonstrated by these observations. Additionally, similar results were observed when activated carbon from mango seeds [75], a Fe_3O_4@ZIF-8 nanocomposite [76], and graphene oxide decorated with silver nanoparticles (GO@AgNPs) [77] were employed to

Table 2
The diffusion parameters estimated for the adsorption of sparfloxacin onto SGO in aqueous solution.

Parameters	[Sparfloxacin]$_0$ (μmol/L)					Temperature (°C)			
	10	25	50	75	100	25	30	35	40
Film Diffusion Model									
$k_{fd} \times 10^{-3}$ (min^{-1})	19.4	20.30	34.50	28.0	28.60	34.50	33.40	31.70	32.60
R^2	0.904	0.873	0.975	0.952	0.953	0.975	0.969	0.958	0.959
Intraparticle Diffusion Model									
k_{id1} (μmol/g $min^{0.5}$)	13.98	26.74	35.79	54.17	80.68	35.79	39.47	42.03	39.98
I_1 (μmol/g)	3.93	23.74	53.91	52.55	45.45	53.91	60.61	61.56	74.28
R^2	0.901	0.959	0.970	0.990	0.974	0.970	0.999	0.999	0.999
k_{id2} (μmol/g $min^{0.5}$)	0.512	0.816	8.04	10.08	11.86	8.04	7.49	5.93	5.34
I_2 (μmol/g)	36.37	104.79	164.22	216.84	269.04	164.22	170.36	181.69	188.92
R^2	0.997	0.977	0.925	0.987	0.933	0.925	0.911	0.828	0.915
k_{id3} (μmol/g $min^{0.5}$)	0.484	0.666	0.577	1.05	1.16	0.577	0.505	0.660	0.422
I_3 (μmol/g)	38.32	107.05	222.79	295.43	354.62	222.79	224.35	223.15	227.03
R^2	0.946	0.917	0.860	0.798	0.933	0.860	0.897	0.896	0.837

remove doxorubicin and metformin from aqueous solutions, respectively.

The formula for the film diffusion model's equation is

$$\ln(1-F) = -k_{fd}t \tag{12}$$

$$F = \frac{q_t}{q_\infty} \tag{13}$$

The rate constant k_{fd} (1/min) is utilized to represent the film diffusion model in the given context. F signifies the fractional attainment of equilibrium. The quantities of sparfloxacin uptake onto SGO at time t and for an infinite amount of time are denoted as q_t (μmol/g) and q_∞ (μmol/g), respectively. The estimation of k_{fd} was derived from the linear relationship between ln(1-F) and t. The findings are presented in Table 2.

The following equation represents the intraparticle diffusion model:

$$q_t = k_{id}t^{0.5} + I \tag{14}$$

In this context, the term k_{id} (μmol/g min$^{0.5}$) refers to the rate constant of the intraparticle diffusion model, while I (μmol/g) denotes the thickness of the boundary layer. The presence of multi-linearity in the q_t versus $t^{0.5}$ plot (Fig. 12) suggests that sparfloxacin is absorbed in three distinct phases. The initial stage, characterized by its high velocity, occurs as a result of sparfloxacin molecules diffusing from the liquid phase to the surface of the SGO via the boundary layer. Subsequently, sparfloxacin molecules enter the pores of the SGO via interior diffusion from the external surface [78]. The terms k_{id1}, k_{id2}, and k_{id3} denote the diffusion rate constants at three distinct phases, as determined by the slope of the corresponding lines in Fig. 12. The diffusion parameters estimated for the adsorption of sparfloxacin onto SGO in aqueous solution are presented in Table 2. The values for k_{id1} are higher than those for k_{id2} and k_{id3} (Table 2), confirming that sparfloxacin was rapidly adsorbed onto the external surface of SGO. The second linear segment indicates the gradual sorption of sparfloxacin, with intraparticle diffusion being the rate-controlling step. The third linear segment corresponds to the final equilibrium, where intraparticle diffusion slows due to the very low concentration of the antibiotic remaining in the solution. These three linear segments show that the sorption of sparfloxacin onto SGO involves both surface sorption and intraparticle diffusion. Additionally, since the values of I are not zero (Table 2), it can be concluded that intraparticle diffusion is not the only rate-controlling step. It was also noted that the adsorption of levofloxacin onto FXM [27] and methylene blue dye onto reduced graphene oxide (rGO) [79] in aqueous solutions occurred in numerous stages at varying rates.

4.7. Activation parameters

The activation energy necessary for sparfloxacin uptake by SGO in an aqueous environment was computed using the k_2 values listed in Table 1, which are associated with different temperatures. Utilizing the provided equation, the activation energy (E_a) was computed [80].

$$\ln k_2 = -\frac{E_a}{RT} + constant \tag{15}$$

where R (8.314 J/mol K) denotes the universal gas constant. The calculation of E_a (27.16 kJ/mol) was performed by analyzing a plot of lnk_2 against $1/T$ ($R^2 = 0.968$). The interaction between the adsorbent and adsorbate can be characterized by the E_a value. The Ea values for chemisorption are 40–800 kJ/mol, while those for physisorption are 5–40 kJ/mol [81]. Therefore, the determined value of E_a (27.16 kJ/mol; Table 1) suggests that physisorption is the mechanism through which sparfloxacin is adsorbed onto SGO.

The equations below were utilized to compute the changes in enthalpy of activation ($\Delta H^{\ddagger}$), entropy of activation ($\Delta S^{\ddagger}$), and Gibbs free energy of activation ($\Delta G^{\ddagger}$) linked to the absorption of sparfloxacin by SGO [73]:

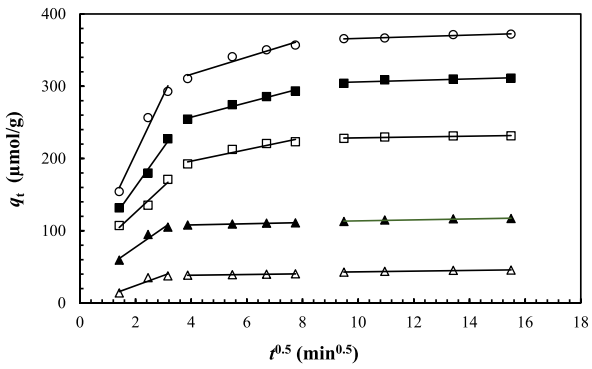

Fig. 12. Characteristic plots of q_t versus $t^{0.5}$ for the adsorption of sparfloxacin onto SGO at different concentrations of sparfloxacin (solution volume: 0.05 L; SGO: 0.010 g; temperature: 25 °C; pH: 5.5; ([Sparfloxacin]$_0$: Δ: 10 μmol/L;: 25 μmol/L; □: 50 μmol/L; ■: 75 μmol/L; ○: 100 μmol/L).

$$\ln\left(\frac{k_2}{T}\right) = -\frac{\Delta H^{\ddagger}}{RT} + \ln\frac{k_B}{h_P} + \frac{\Delta S^{\ddagger}}{R} \tag{16}$$

$$\Delta G^{\ddagger} = \Delta H^{\ddagger} - T\Delta S^{\ddagger} \tag{17}$$

where k_2 (g/mol min), R, and T have equal relevance as stated previously, h_P (6.626×10^{-34} Js) and k_B (1.381×10^{-23} J/K) represent the Planck constant and Boltzman constant, respectively. The values of $\Delta H^{\ddagger}$ and $\Delta S^{\ddagger}$ were derived by determining the slope and y-intercept of the plot $\ln(k_2/T)$ vs $1/T$, with an R^2 value of 0.961. The estimated value of $\Delta H^{\ddagger}$ is 24.62 kJ/mol (Table 1), which is consistent with the properties of an endothermic diffusion process. The calculated value of $\Delta S^{\ddagger}$, −102.29 J/mol K (Table 1), suggests that the internal structure of the adsorbent material remained largely unchanged during the adsorption process. The values of $\Delta G^{\ddagger}$ were found to be 55.62, 56.13, 56.64, and 57.15 kJ/mol (Table 1) at temperatures of 25, 30, 35, and 40 °C, respectively. A positive value of $\Delta G^{\ddagger}$ indicates the presence of an energy barrier during the adsorption process [73]. Similar findings were recorded for the adsorption of cefixime onto chitosan in an aqueous solution [38].

4.8. Adsorption isotherm

The isotherm analysis is used to characterize both the adsorption capacity and the attraction between the adsorbate and adsorbent. The adsorption mechanism was elucidated by utilizing experimental isotherm data in conjunction with widely used isotherm equations. Fig. 13 illustrates the relationship between q_e and C_e at various solution temperatures. The observation was made that the degree of equilibrium sparfloxacin adsorption onto SGO increased as the solution temperature increased (Fig. 13a–d). This indicates that the adsorption of sparfloxacin is an endothermic process. To provide an explanation, experimental data collected at different temperatures were analyzed utilizing the isotherm equations proposed by Freundlich [82], Temkin [83], Dubinin–Radushkevich [84], and Langmuir [85]. The following are the linear and non-linear representations of the isotherm models:

Freundlich model:

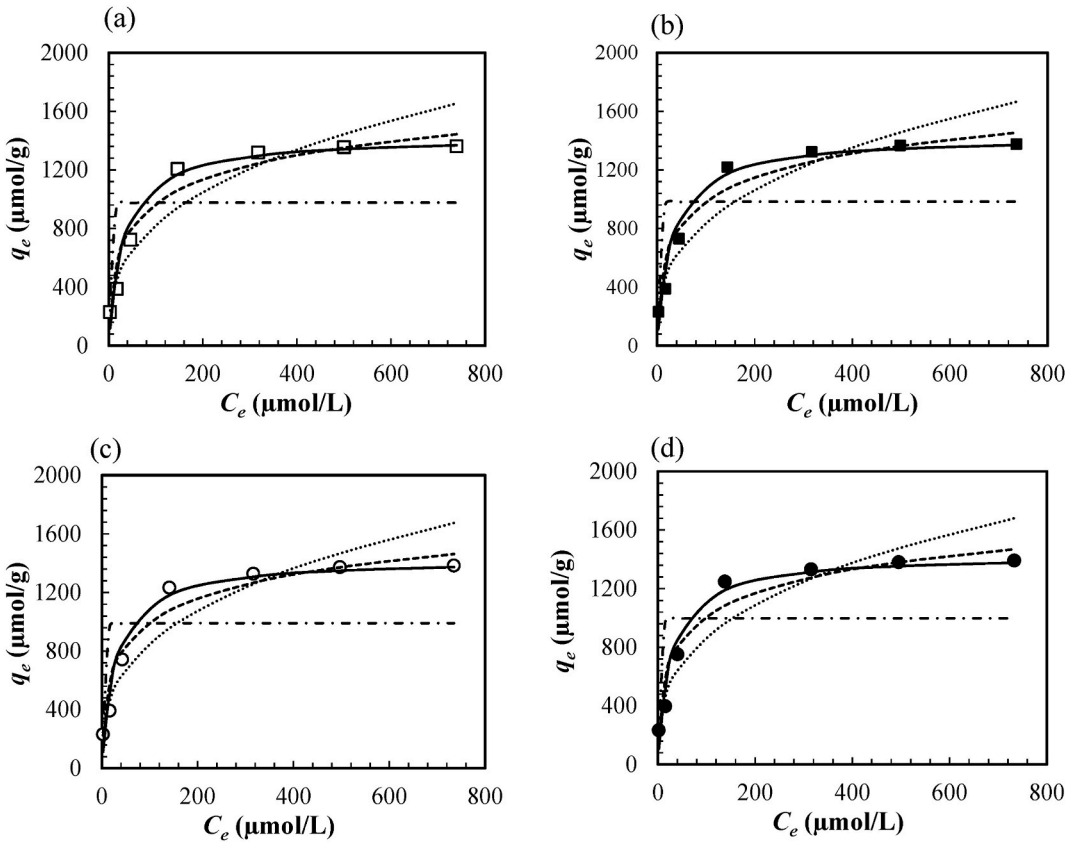

Fig. 13. Illustrates the equilibrium adsorption isotherm of sparfloxacin onto SGO in aqueous solution (pH 5.5) at different temperatures (a) □: 25 °C; (b) ■: 30 °C; (c) ○: 35 °C; and (d) ●: 40 °C ($[\text{Sparfloxacin}]_0$: 50–1000 µmol/L; solution volume: 0.05 L; SGO: 0.010 g). The Freundlich (…), Tempkin (—), Dubinin-Radushkevich (.-.-), and Langmuir isotherm (– –) equations and the values of isotherm constants (Table 3) were employed to simulate all lines.

Nonlinear form $q_e = K_F C_e^{\frac{1}{n}}$ (18)

Linear form $ln\ q_e = \frac{1}{n} ln\ C_e + ln\ K_F$ (19)

Temkin model:

Nonlinear form $q_e = \frac{RT}{b} ln(K_T C_e)$ (20)

Linear form $q_e = \frac{RT}{b} \ln K_T + \frac{RT}{b} ln\ C_e$ (21)

Dubinin-Radushkevich model:

Nonlinear form $q_e = q_{DR}\ \exp\left(-K_{DR}\varepsilon^2\right)$ (22)

Linear form $lnq_e = lnq_{DR}\ - K_{DR}\varepsilon^2$ (23)

$\varepsilon = RT \ln\left(1 - \frac{1}{C_e}\right)$ (24)

$E = \frac{1}{(2K_{DR})^{0.5}}$ (25)

Langmuir model:

Nonlinear form $q_e = \frac{K_L C_e}{(1 + a_L C_e)}$ (26)

Linear form $\frac{C_e}{q_e} = \frac{1}{K_L} + \frac{a_L}{K_L} C_e$ (27)

In the given context, C_e (μmol/L) represents the equilibrium concentration of sparfloxacin in solution, q_e (μmol/g) represents the quantity of sparfloxacin adsorbed per unit weight of SGO at equilibrium time, and K_F ((μmol/g) (μmol/L)$^{-1/n}$) and n are Freundlich

Table 3
Isotherm and thermodynamic parameters for the adsorption of sparfloxacin onto SGO at different temperatures.

Parameters	Temperature (°C)			
	25	30	35	40
Freundlich Isotherm Model				
K_F ((μmol/g) (μmol/L)$^{-1/n}$)	165.47	172.05	178.07	186.51
n	2.87	2.91	2.94	3.00
R^2	0.959	0.960	0.960	0.961
RMSE	191.89	191.29	195.29	196.95
Temkin Isotherm Model				
K_T (μmol/L)	0.602	0.658	0.714	0.803
b (J/mol)	10.46	10.71	10.96	11.30
R^2	0.947	0.946	0.946	0.945
RMSE	122.75	125.43	125.44	127.43
Dubinin-Radushkevich Isotherm Model				
q_{DR} (μmol/g)	976.53	983.48	990.89	997.55
$K \times 10^{-6}$ (J^2/mol^2)	1.00	1.00	0.90	0.70
E (kJ/mol)	0.71	0.71	0.75	0.85
R^2	0.595	0.592	0.595	0.596
RMSE	414.81	415.40	415.54	417.46
Langmuir Isotherm Model				
K_L (L/g)	43.86	45.45	48.31	51.55
$a_L \times 10^{-3}$ (L/μmol)	30.70	31.82	33.82	36.08
q_m (μmol/g)	1428.57	1428.57	1428.57	1428.57
R^2	0.998	0.998	0.999	0.999
RMSE	89.84	91.52	90.99	93.13
Thermodynamic Study				
ΔG (kJ/mol)	−25.60	−26.12	−26.70	−27.31
ΔH (kJ/mol)	8.44			
ΔS (J/mol K)	114.15			
R^2	0.981			

constants that are associated with the capacity of adsorption and adsorption intensities, respectively [78]. The Temkin constant is denoted by K_T (μmol/L), while b (J/mol) is a constant associated with the heat of adsorption. ε represents the polanyi potential, E (kJ/mol) denotes the mean adsorption energy, K_{DR} (J^2/mol^2) indicates the Dubinin-Radushkevich constant, and q_{DR} (μmol/g) signifies the maximum adsorption capacity. K_L (L/g) and a_L (L/μmol) represent the Langmuir isotherm constants, where the ratio of K_L/a_L indicates the maximum antibiotic adsorption capacity, q_m (μmol/g). T and R have the identical meaning as stated previously.

A comparative analysis was conducted between the experimental and theoretical isotherm data obtained from the Freundlich, Tempkin, Dubinin-Radushkevich, and Langmuir isotherm models for sparfloxacin adsorption onto SGO (Fig. 13a–d). The values of isotherm constants were obtained from linearized isotherm models (figures not provided). The parameters of various isotherm models are shown in Table 3. The values of K_F exhibited a positive correlation with increasing temperatures within the range of 25–40 °C, suggesting that the uptake of sparfloxacin is characterized by an endothermic process. The values of n were determined to be 2.87, 2.91, 2.94, and 3.00 at temperatures of 25, 30, 35, and 40 °C, respectively. These values indicate that the adsorption process is favorable. The K_T values (0.602 μmol/L, 0.658 μmol/L, 0.714 μmol/L, and 0.803 μmol/L) and b values (10.46 J/mol, 110.71 J/mol, 10.96 J/mol, and 11.30 J/mol) were determined at 25, 30, 35, and 40 °C, respectively, from the intercepts and slopes of the plots of q_e *vs*. lnC_e (Figure not provided). The b values indicated that the adsorption of sparfloxacin onto SGO was an endothermic process [29]. According to the Dubinin-Radushkevich model, the calculated E values were 0.71 kJ/mol, 0.71 kJ/mol, 0.75 kJ/mol, and 0.85 kJ/mol at 25, 30, 35, and 40 °C, respectively, suggesting that the antibiotic adsorption onto SGO predominantly involves physical adsorption [29,63,66]. By comparing the RMSE and the R^2 values obtained from the Freundlich, Temkin, Dubinin-Radushkevich, and Langmuir models, it can be concluded that the experimental isotherm data were well-fitted to the Langmuir model. As indicated in Table 3, the values of a_L and K_L increased with the rise in solution temperature from 25 to 40 °C. These findings also imply that the SGO-sparfloxacin interaction is likely an endothermic process [66]. The maximum uptake capacity (q_m) of sparfloxacin on SGO was found to be 1428.57 μmol/g at 25 °C using the Langmuir equation. The similar results were observed when sawdust treated with hexadecylpyridinium bromide was used to remove Allura Red AC from an aqueous solution [63].

The comparative analysis of the adsorption capacities of SGO and other adsorbents documented in the literature for sparfloxacin is presented in Table 4. The results demonstrate that SGO has a higher capacity for sparfloxacin adsorption compared to alternative adsorbents such as CP/SDS [21], SA-Ca/Cu [22], mGOCP [23], and GO@Fe3O4 [24]. Therefore, SGO is recommended as an efficient and economical adsorbent for removing sparfloxacin from aqueous solutions.

4.9. Thermodynamics

It is imperative to conduct a thermodynamic analysis of the adsorption process to determine whether the system operates spontaneously. The calculations for thermodynamic variables, including changes in Gibb's free energy (ΔG, kJ/mol), enthalpy (ΔH, kJ/mol), and entropy (ΔS, J/mol K), were performed using the Langmuir isotherm constant (a_L, L/mol) and the equations that followed [67].

$$\Delta G = -RT \ln a_L \tag{28}$$

$$ln\, a_L = \frac{\Delta S}{R} - \frac{\Delta H}{RT} \tag{29}$$

where R (8.314 J/mol K) and T (K) remain the same as before. The estimation of ΔH and ΔS during the adsorption process was conducted by analyzing the y-intercept and slope of the plot of $\ln a_L$ versus $1/T$ ($R^2 = 0.981$). Table 3 presents the thermodynamic values that have been estimated. The negative values of ΔG: −25.60 to −27.31 kJ/mol indicate that the adsorption process is feasible and spontaneous in nature. Conversely, the positive value of ΔH: 8.44 kJ/mol provides evidence that the adsorption process is endothermic. The positive ΔS value 114.15 J/mol K indicates that sparfloxacin molecules exhibited a strong affinity for the SGO surface. The existence of randomness at the solid-liquid interface during sparfloxacin adsorption onto SGO is demonstrated by the positive ΔS values. This randomness results from the translational entropy generated by the water molecules being exchanged, which is associated with the energy lost due to antibiotic adsorption [63].

4.10. Desorption and reuse of SGO

Regeneration, reusability, and stability of the adsorbent are essential qualities in the development of a cost-effective adsorption process. Fig. 14 illustrates the customary adsorption-desorption-adsorption cycle of sparfoxacin onto SGO in aqueous solution. During the adsorption process, a 50 μmol/L solution of sparfoxacin was utilized, which was maintained at a temperature of 25 °C and a working solution pH of 5.5 (Fig. 14a). The release of sparfoxacin from the adsorbent containing the antibiotic was observed in a DMF solution containing 1 mol/L HCl (Fig. 14a), also at a temperature of 25 °C. The intensity of equilibrium sparfloxacin adsorption during the initial adsorption phase was calculated to be 231.96 μmol/g (Fig. 14a). The rapid desorption rate of the initial antibiotic was noted, with 89.42 % of sparfloxacin being liberated within a 15-min time span. Within 240 min, 91 % of sparfloxacin was liberated from the antibiotic-containing adsorbent. This is because the electrostatic interaction between the adsorbent and the sparfloxacin molecules was considerably weakened in a highly acidic DMF solution. The observed phenomenon may also be ascribed to the replacement of protonated sparfloxacin molecules adsorbed onto the SGO surface in the highly acidic medium with hydronium ions (H_3O^+). In addition, the methyl group (-CH_3) of DMF is firmly deposited on the hydrophobic portion of SGO, while the carbonyl group (C=O) of

Table 4
A comparative analysis of the absorption capacities of different adsorbents in an aqueous environment to remove sparfloxacin.

Adsorbent	pH	Temperature (°C)	$q_{m.}$ (μmol/g)	Reference
CP/SDS	5.0	25	24.21	21
SA-Ca/Cu	7.0	55	726.28	22
mGOCP	6.0	25	1280.22	23
GO@Fe_3O_4	7.0	25	163.09	24
SGO	5.5	25	1428.57	Present Study

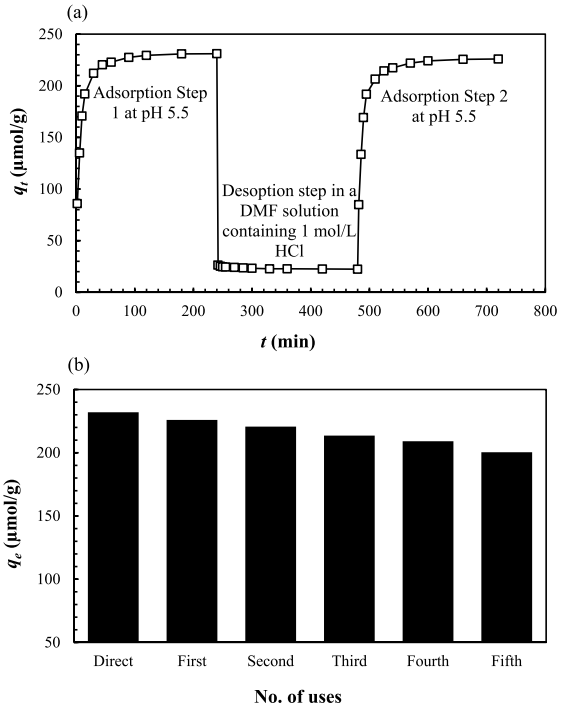

Fig. 14. (a) Kinetic graph of the cycle of sparfloxacin adsorption and desorption at 25 °C and 50 μmol/L sparfloxacin with three steps: adsorption step 1 at initial pH 5.5, desorption step in a DMF solution containing 1 mol/L HCl, and adsorption step 2 at initial pH 5.5. (b) The impact of regeneration cycles on the adsorption capacity of sparfloxacin at standard conditions (50 μmol/L sparfloxacin, 0.05 L solution volume, 0.01 g SGO, 25 °C temperature, pH 5.5).

DMF interacts with the hydrophilic portion of SGO. Potentially, these interactions facilitate the desorption of sparfloxacin molecules by acting as a catalyst [86,87]. Subsequent to the antibiotic-releasing step, sparfloxacin was adsorbed, revealing adsorption phenomena comparable to those observed in the initial adsorption phase. Similar levels of sparfloxacin adsorption were detected in the second adsorption phase. The findings indicate that the current adsorbent SGO has the potential to be utilized again in the adsorption of sparfloxacin. The q_e values obtained from direct use analysis were as follows: 231.99, 225.95, 220.61, 213.53, 209.05, and 200.40 μmol/g for the initial, first, second, third, fourth, and fifth regenerations, respectively (Fig. 14b). The gradual decrease in adsorption capacity after each adsorption-desorption cycle can be ascribed to various factors, including pore blockage of the adsorbent, reduction in the number of active binding sites, and depletion of the adsorbent level [88]. According to the findings of this investigation, SGO could potentially function as a feasible adsorbent substance in order to extract sparfloxacin from aquatic ecosystems.

5. Conclusions

The current investigation showcases the fabrication process of SGO and its practical implementation in the removal of sparfloxacin from an aqueous solution. UV–Vis spectroscopy, FT-IR, XPS, SEM, TEM, EDX, particle size, and TGA were utilized to characterize SGO. The pH_{zpc} value of SGO was determined through the pH drift method to be 2.5. It was ascertained that the BET surface area of SGO is 32.25 m^2/g. The experimental findings indicate that the affinity of sparfloxacin for SGO is pH-dependent. The enhancement of sparfloxacin absorption capacity was observed as the interaction time, concentration, and temperature of the solution increased, respectively. The adsorption process is characterized by the pseudo-second-order kinetic model and the Langmuir isotherm model, according to the kinetic and isotherm results. The highest adsorption of sparfloxacin onto SGO was determined to be 1428.57 μmol/g

in aqueous solutions (pH 5.5) at 25 °C. The thermodynamic variables (ΔH: 8.44 kJ/mol; ΔS: 114.15 J/mol.K; and ΔG: −25.60 to −27.31 kJ/mol) provide evidence supporting the conclusion that the process of antibiotic uptake onto SGO is spontaneous and endothermic. The E_a value (27.16 kJ/mol) indicates that the adsorption process exhibits physisorption characteristics. In a DMF solution containing 1 mol/L HCl, sparfloxacin desorption from sparfloxacin-loaded SGO was determined to be 91 %. In order to assess the reusability and stability of SGO, five to six adsorption-desorption experiments were conducted. Drawing from the empirical and theoretical calculations, it is possible to deduce that SGO possesses the capability to function as an effective adsorbent in the removal of sparfloxacin from aquatic environments.

CRediT authorship contribution statement

Chironjit Kumar Shaha: Writing – original draft, Methodology, Formal analysis, Data curation. **Md Abdullah Al Mahmud:** Methodology, Formal analysis, Data curation. **Sudipta Saha:** Writing – original draft, Methodology, Formal analysis, Data curation. **Subarna Karmaker:** Writing – review & editing, Writing – original draft, Supervision, Funding acquisition, Conceptualization. **Tapan Kumar Saha:** Writing – review & editing, Writing – original draft, Supervision, Funding acquisition, Data curation, Conceptualization.

Declaration of competing interest

The authors declare the following financial interests/personal relationships which may be considered as potential competing interests:Tapan Kumar Saha reports financial support was provided by Alexander von Humboldt Foundation. Not Applicable If there are other authors, they declare that they have no known competing financial interests or personal relationships that could have appeared to influence the work reported in this paper.

Acknowledgments

We express our sincere appreciation for the assistance rendered by the Alexander von Humboldt Foundation (ref.34-8151/T.K.S. (GA-Nr. 20 007)) in Germany and the Ministry of Science and Technology, Government of the People's Republic of Bangladesh (T.K.S. and S.K.). We are also appreciative of the Wazed Miah Science Research Center, Jahangirnagar University, and the Bangladesh Council of Scientific and Industrial Research (BCSIR), Dhaka for providing us with the opportunity to analyze the samples using FTIR, powder XRD, BET, and laser diffraction particle size analyzer systems.

Appendix A. Supplementary data

Supplementary data to this article can be found online at https://doi.org/10.1016/j.heliyon.2024.e33644.

References

[1] M.M. Mehanni, S.I. Gadow, F.A. Alshammari, Y. Modafer, K.Z. Ghanem, N.F. El-Tahtawi, R.F. El-Homosy, A.E. Hesham, Antibiotic-resistant bacteria in hospital wastewater treatment plant effluent and the possible consequences of its reuse in agricultural irrigation, Front. Microbiol. 14 (2023) 1141383.
[2] A. Kock, H. Glanville, A. Law, T. Stanton, L. Carter, J. Taylor, Emerging challenges of the impacts of pharmaceuticals on aquatic ecosystems: a diatom perspective, Sci. Total Environ. 878 (2023) 162939.
[3] E. Zuccato, D. Calamari, M. Natangelo, R. Fanelli, Presence of therapeutic drugs in the environment, Lancet 355 (2000) 1789–1790.
[4] M. Sharma, K. Kumar, K.K. Dubey, Disposal of unused antibiotics as household waste: a social driver of antimicrobial resistance, Environ. Qual. Manag. 30 (2021) 127–140.
[5] Z. Maghsodian, A.M. Sanati, T. Mashifana, M. Sillanpää, S. Feng, T. Nhat, B. Ramavandi, Occurrence and distribution of antibiotics in the water, sediment, and biota of freshwater and marine environments: a review, Antibiotics 11 (2022) 1461.
[6] L. Chen, H. Lang, F. Liu, S. Jin, T. Yan, Presence of antibiotics in shallow groundwater in the northern and southwestern regions of China, Groundwater 56 (2018) 451–457.
[7] B.W. Grehs, M.A. Linton, B. Clasen, A. de Oliveira Silveira, E. Carissimi, Antibiotic resistance in wastewater treatment plants: understanding the problem and future perspectives, Arch. Microbiol. 203 (2021) 1009–1020.
[8] W.-L. Jia, C. Song, L.-Y. He, B. Wang, F.-Z. Gao, M. Zhang, G.-G. Ying, Antibiotics in soil and water: occurrence, fate, and risk, Curr. Opin. Environ. Sci. Health 32 (2022) 100437.
[9] P.S. McManus, V.O. Stockwell, G.W. Sundin, A.L. Jones, Antibiotic use in plant agriculture, Annu. Rev. Phytopathol. 40 (2002) 443–465.
[10] P. Taylor, R. Reeder, Antibiotic use on crops in low and middle-income countries based on recommendations made by agricultural advisors, CABI Agric. Biosci. 1 (2020) 1–14.
[11] K. Muaz, M. Riaz, S. Akhtar, S. Park, A. Ismail, Antibiotic residues in chicken meat: global prevalence, threats, and decontamination strategies: a review, J. Food Protect. 81 (2018) 619–627.
[12] D. Chakma, M.M.B. Prince, M.H. Islam, E. Tanvir, M.M. Nabi, W. Reybroeck, J.J. Sasanya, M.J. Islam, M.N. Islam, M.S.U. Talukder, C.K. Shaha, M.A. Mannan, A. S.M. Saifullah, Screening for antimicrobial residues in poultry eggs in Bangladesh using Charm II radio-receptor assay technique following validation, Food Addit. Contam. Part B Surveill. 16 (2023) 288–300.
[13] S. Sachi, J. Ferdous, M.H. Sikder, S.A.K. Hussani, Antibiotic residues in milk: past, present, and future, J. Adv. Vet. Anim. Res. 6 (2019) 315–332.
[14] P.A. Evangelista, F.M.d.O. Lourenço, D. Chakma, C.K. Shaha, A. Konate, R.F. Pimpinato, H. Louvandini, V.L. Tornisielo, Bioaccumulation and depletion of the antibiotic sulfadiazine ^{14}C in lambari (*Astyanax bimaculatus*), Animals 13 (2023) 2464.
[15] X. Van Doorslaer, J. Dewulf, H. Van Langenhove, K. Demeestere, Fluoroquinolone antibiotics: an emerging class of environmental micropollutants, Sci. Total Environ. 500–501 (2014) 250–269.
[16] B. Hamad, The antibiotics market, Nat. Rev. Drug Discov. 9 (2010) 675–676.

[17] S. Bhatt, S. Chatterjee, Fluoroquinolone antibiotics: occurrence, mode of action, resistance, environmental detection, and remediation–A comprehensive review, Environ. Pollut. 315 (2022) 120440.
[18] A. Ashiq, M. Vithanage, B. Sarkar, M. Kumar, A. Bhatnagar, E. Khan, Y. Xi, Y.S. Ok, Carbon-based adsorbents for fluoroquinolone removal from water and wastewater: a critical review, Environ. Res. 197 (2021) 111091.
[19] N. Chansud, R. Kaewnok, P. Nurerk, F. Davis, O.J.M.T.C. Bunkoed, Ultrasensitive and highly selective fluorescence probe of nitrogen-doped graphene quantum dots and zinc oxide decorated carbon foam incorporated molecularly imprinted polymer for trace sparfloxacin determination, Mater. Today Commun. 35 (2023) 105687.
[20] J. Kurasam, P. Sihag, P.K. Mandal, S. Sarkar, Presence of fluoroquinolone resistance with persistent occurrence of gyrA gene mutations in a municipal wastewater treatment plant in India, Chemosphere 211 (2018) 817–825.
[21] S. Dong, Q. Zheng, G. Huang, X. Wang, T.J.I. Huang, E.C. Research, The coordination polymer [Cu (bipy)$(SO_4)]_n$ and its functionalization for selective removal of two types of organic pollutants, Ind. Eng. Chem. Res. 58 (2019) 15416–15424.
[22] Y. Wang, H. Wang, L. Li, L. Jia, Fabrication of calcium/cupric crosslinked alginate electrospun nanofibers for enhancing fluoroquinolones adsorption, Microporous Mesoporous Mater. 336 (2022) 111857.
[23] Y. Zhou, S. Cao, C. Xi, X. Li, L. Zhang, G. Wang, Z. Chen, A novel Fe_3O_4/graphene oxide/citrus peel-derived bio-char based nanocomposite with enhanced adsorption affinity and sensitivity of ciprofloxacin and sparfloxacin, Bioresour. Technol. 292 (2019) 121951.
[24] R.E.A. Mohammad, A.A. Elbashir, J. Karim, N. Yahaya, N.Y. Rahim, M. Miskam, Adsorptive performances of magnetic graphene oxide adsorbent for the removal of fluoroquinolones in the Langat River Basin, Malaysia, Int. J. Environ. Anal. Chem. 103 (2023) 6475–6494.
[25] M.M. Sabzehmeidani, S. Mahnaee, M. Ghaedi, H. Heidari, V.A.L. Roy, Carbon based materials: a review of adsorbents for inorganic and organic compounds, Mater. Adv. 2 (2021) 598–627.
[26] S. Thangavel, G. Venugopal, Understanding the adsorption property of graphene-oxide with different degrees of oxidation levels, Powder Technol. 257 (2014) 141–148.
[27] N. Rahman, A. Raheem, Mechanistic investigation of levofloxacin adsorption on Fe(III)-tartaric acid/xanthan gum/graphene oxide/polyacrylamidehydrogel: box-Behnken design and Taguchi method for optimization, J. Ind. Eng. Chem. 127 (2023) 110–124.
[28] N. Rahman, A. Raheem, Fabrication of graphene oxide/inulin impregnated with ZnO nanoparticles for efficient removal of enrofloxacin from water: taguchi-optimized experimental analysis, J. Environ. Manag. 318 (2022) 115525.
[29] N. Rahman, P. Varshney, Facile synthesis and characterization of Zn(II)-impregnated chitosan/graphene oxide: evaluation of its efficiency for removal of ciprofloxacin from aqueous solution, J. Inorg. Organomet. Polym. Mater. 31 (2021) 3595–3612.
[30] A. Tawfik, M. Eraky, M.N. Khalil, A.I. Osman, D.W. Rooney, Sulfonated graphene nanomaterials for membrane antifouling, pollutant removal, and production of chemicals from biomass: a review, Environ. Chem. Lett. 21 (2023) 1093–1116.
[31] Q. Hou, W. Li, M. Ju, L. Liu, Y. Chen, Q. Yang, One-pot synthesis of sulfonated graphene oxide for efficient conversion of fructose into HMF, RSC Adv. 6 (2016) 104016–104024.
[32] M.-p. Wei, H. Chai, Y.-l. Cao, D.-z. Jia, Sulfonated graphene oxide as an adsorbent for removal of Pb2+ and methylene blue, J. Colloid Interface Sci. 524 (2018) 297–305.
[33] D.C. Marcano, D.V. Kosynkin, J.M. Berlin, A. Sinitskii, Z. Sun, A. Slesarev, L.B. Alemany, W. Lu, J.M. Tour, Improved synthesis of graphene oxide, ACS Nano 4 (2010) 4806–4814.
[34] V.R. Moreira, Y.A.R. Lebron, M.M. da Silva, L.V. de Souza Santos, R.S. Jacob, C.K.B. de Vasconcelos, M.M. Viana, Graphene oxide in the remediation of norfloxacin from aqueous matrix: simultaneous adsorption and degradation process, Environ. Sci. Pollut. Res. 27 (2020) 34513–34528.
[35] M.N. Khan, A. Sarwar, Determination of points of zero charge of natural and treated adsorbents, Surf. Rev. Lett. 14 (2007) 461–469.
[36] Y.S. Kim, S.J. Yang, H.J. Lim, T. Kim, C.R.J.C. Park, A simple method for determining the neutralization point in Boehm titration regardless of the CO_2 effect, Carbon 50 (9) (2012) 3315–3323.
[37] P. Basak, S. Dey, P. Ghosh, Sulfonated graphene-oxide as metal-free efficient carbocatalyst for the synthesis of 3-methyl-4-(hetero)arylmethylene isoxazole-5 (4H)-ones and substituted pyrazole, ChemistrySelect 5 (2020) 626–636.
[38] G.M.S. Uddin, S. Saha, S. Karmaker, T.K. Saha, Adsorption of cefixime trihydrate onto chitosan 10B from aqueous solution: kinetics, equilibrium and thermodynamic studies, Cellul. Chem. Technol. 55 (2021) 771–784.
[39] H. Zhang, H.M. Selim, Kinetics of arsenate adsorption– desorption in soils, Environ. Sci. Technol. 39 (2005) 6101–6108.
[40] E. Aliyev, V. Filiz, M.M. Khan, Y.J. Lee, C. Abetz, V. Abetz, Structural characterization of graphene oxide: surface functional groups and fractionated oxidative debris, Nanomaterials 9 (2019) 1180.
[41] D. Khalili, Graphene oxide: a promising carbocatalyst for the regioselective thiocyanation of aromatic amines, phenols, anisols and enolizable ketones by hydrogen peroxide/KSCN in water, New J. Chem. 40 (2016) 2547–2553.
[42] D. Li, M.B. Müller, S. Gilje, R.B. Kaner, G.G. Wallace, Processable aqueous dispersions of graphene nanosheets, Nat. Nanotechnol. 3 (2008) 101–105.
[43] V. Gupta, N. Sharma, U. Singh, M. Arif, A. Singh, Higher oxidation level in graphene oxide, Optik 143 (2017) 115–124.
[44] Z. Ciğeroğlu, O.K. Özdemir, S. Şahin, A. Haşimoğlu, Naproxen adsorption onto graphene oxide nanopowders: equilibrium, kinetic, and thermodynamic studies, Water Air Soil Pollut. 231 (2020) 1–10.
[45] M. Acik, C. Mattevi, C. Gong, G. Lee, K. Cho, M. Chhowalla, Y. Chabal, The role of intercalated water in multilayered graphene oxide, ACS Nano 4 (2010) 5861–5868.
[46] R. Kumar, M. Mamlouk, K.R.A. Scott, Sulfonated polyether ether ketone–sulfonated graphene oxide composite membranes for polymer electrolyte fuel cells, RSC Adv. 4 (2014) 617–623.
[47] S. Ayyaru, Y.-H. Ahn, Application of sulfonic acid group functionalized graphene oxide to improve hydrophilicity, permeability, and antifouling of PVDF nanocomposite ultrafiltration membranes, J. Membr. Sci. 525 (2017) 210–219.
[48] I.K. Basha, E.M. Abd El-Monaem, R.E. Khalifa, A.M. Omer, A.S. Eltaweil, Sulfonated graphene oxide impregnated cellulose acetate floated beads for adsorption of methylene blue dye: optimization using response surface methodology, Sci. Rep. 12 (2022) 9339.
[49] R. Al-Gaashani, A. Najjar, Y. Zakaria, S. Mansour, M. Atieh, XPS and structural studies of high quality graphene oxide and reduced graphene oxide prepared by different chemical oxidation methods, Ceram. Int. 45 (2019) 14439–14448.
[50] A. Arabpour, S. Dan, H. Hashemipour, Preparation and optimization of novel graphene oxide and adsorption isotherm study of methylene blue, Arab. J. Chem. 14 (2021) 103003.
[51] G. Zhao, X. Ren, X. Gao, X. Tan, J. Li, C. Chen, Y. Huang, X. Wang, Removal of Pb (II) ions from aqueous solutions on few-layered graphene oxide nanosheets, Dalton Trans. 40 (2011) 10945–10952.
[52] S. Muralikrishna, K. Sureshkumar, T.S. Varley, D.H. Nagaraju, T. Ramakrishnappa, In situ reduction and functionalization of graphene oxide with L-cysteine for simultaneous electrochemical determination of cadmium (II), lead (II), copper (II), and mercury (II) ions, Anal. Methods 6 (2014) 8698–8705.
[53] P.M. Shanthi, P.J. Hanumantha, K. Ramalinga, B. Gattu, M.K. Datta, P.N. Kumta, Sulfonic acid based complex framework materials (CFM): nanostructured polysulfide immobilization systems for rechargeable lithium–sulfur battery, J. Electrochem. Soc. 166 (2019) A1827–A1835.
[54] A. Munir, T.u. Haq, A. Qurashi, H.U. Rehman, A. Ul-Hamid, I. Hussain, Ultrasmall Ni/NiO nanoclusters on thiol-functionalized and-exfoliated graphene oxide nanosheets for durable oxygen evolution reaction, ACS Appl. Energy Mater. 2 (2018) 363–371.
[55] Z. Zhang, H.C. Schniepp, D.H. Adamson, Characterization of graphene oxide: variations in reported approaches, Carbon 154 (2019) 510–521.
[56] L. Stobinski, B. Lesiak, A. Malolepszy, M. Mazurkiewicz, B. Mierzwa, J. Zemek, P. Jiricek, I. Bieloshapka, Graphene oxide and reduced graphene oxide studied by the XRD, TEM and electron spectroscopy methods, J. Electron. Spectrosc. Relat. Phenom. 195 (2014) 145–154.
[57] R.G. Abaszade, Synthesis and analysis of flakes graphene oxide, J. Optoelectron. Biomed. Mater. 14 (2022) 107–114.
[58] Ravikumar, K. Scott, Freestanding sulfonated graphene oxide paper: a new polymer electrolyte for polymer electrolyte fuel cells, Chem. Commun. 48 (2012) 5584–5586.

[59] S. Bele, V. Samanidou, E. Deliyanni, Effect of the reduction degree of graphene oxide on the adsorption of Bisphenol A, Chem. Eng. Res. Des. 109 (2016) 573–585.
[60] E. Wolak, A. Orzechowska-Zięba, Change of the surface and structure of activated carbon as a result of HNO_3 modification, Adsorption 30 (2024) 121–128.
[61] O.O. Oluwasina, A.A. Adelodun, O.O. Oluwasina, H.A. Duarte, S.J. Olusegun, Experimental and computational studies of crystal violet removal from aqueous solution using sulfonated graphene oxide, Sci. Rep. 14 (2024) 6207.
[62] X. Zhang, J. Shen, N. Zhuo, Z. Tian, P. Xu, Z. Yang, W. Yang, Interactions between antibiotics and graphene-based materials in water: a comparative experimental and theoretical investigation, ACS Appl. Mater. Interfaces 8 (2016) 24273–24280.
[63] T.K. Saha, R.K. Bishwas, S. Karmaker, Z. Islam, Adsorption characteristics of allura red AC onto sawdust and hexadecylpyridinium bromide-treated sawdust in aqueous solution, ACS Omega 5 (2020) 13358–13374.
[64] X.S. Wang, J.P. Chen, Removal of the azo dye Congo red from aqueous solutions by the marine alga Porphyra yezoensis Ueda, Clean: Soil, Air, Water 37 (2009) 793–798.
[65] H. Shi, W. Li, L. Zhong, C. Xu, Methylene blue adsorption from aqueous solution by magnetic cellulose/graphene oxide composite: equilibrium, kinetics, and thermodynamics, Ind. Eng. Chem. Res. 53 (2014) 1108–1118.
[66] S. Karmaker, A.J. Nag, T.K. Saha, Adsorption of remazol brilliant violet onto chitosan 10B in aqueous solution: kinetics, equilibrium and thermodynamics studies, Cellul. Chem. Technol. 53 (2019) 373–386.
[67] T.K. Saha, N.C. Bhoumik, S. Karmaker, M.G. Ahmed, H. Ichikawa, Y. Fukumori, Adsorption characteristics of reactive black 5 from aqueous solution onto chitosan, Clean: Soil, Air, Water 39 (2011) 984–993.
[68] K. Yang, B. Chen, X. Zhu, B. Xing, Aggregation, adsorption, and morphological transformation of graphene oxide in aqueous solutions containing different metal cations, Environ. Sci. Technol. 50 (2016) 11066–11075.
[69] V. Sabna, S.G. Thampi, S. Chandrakaran, Adsorptive removal of cationic and anionic dyes using graphene oxide, Water Sci. Technol. 78 (2018) 732–742.
[70] S. Lagergren, Zur theorie der sogenannten adsorption geloster stoffe, K. Sven. Vetenskapsakad. Handl. (24) (1898) 1–39.
[71] Y.S. Ho, G. McKay, Pseudo-second order model for sorption processes, Process Biochem. 34 (1999) 451–465.
[72] S.Y. Elovich, O.G. Larionov, Theory of adsorption from nonelectrolyte solutions on solid adsorbents, Russ. Chem. Bull. 11 (1962) 198–203.
[73] S. Karmaker, T. Sen, T.K. Saha, Adsorption of reactive yellow 145 onto chitosan in aqueous solution: kinetic modeling and thermodynamic analysis, Polym. Bull. 72 (2015) 1879–1897.
[74] W.J. Weber, J.C. Morris, Kinetics of adsorption on carbon from solution, J. Sanit. Eng. Div. 89 (1963) 31–60.
[75] T.A. Altalhi, M.M. Ibrahim, G.A.M. Mersal, M.H.H. Mahmoud, T. Kumeria, M.G. El-Desouky, A.A. El-Bindary, M.A. El-Bindary, Adsorption of doxorubicin hydrochloride onto thermally treated green adsorbent: equilibrium, kinetic and thermodynamic studies, J. Mol. Struct. 1263 (2022) 133160.
[76] G.A.A. Al-Hazmi, A.A. El-Zahhar, M.G. El-Desouky, M.A. El-Bindary, A.A. El-Bindary, Efficiency of Fe_3O_4@ZIF-8 for the removal of Doxorubicin from aqueous solutions: equilibrium, kinetics and thermodynamic studies, Environ. Technol. 45 (2024) 731–750.
[77] N. Rahman, M. Bharti, M. Nasir, S.N.H. Azmi, Performance assessment of graphene oxide decorated with silver nanoparticles as adsorbent for removal of metformin from water: equilibrium modeling, kinetic and thermodynamic studies, Materials 3 (2024) 100046.
[78] C. Duran, D. Ozdes, A. Gundogdu, H.B. Senturk, Kinetics and isotherm analysis of basic dyes adsorption onto almond shell (Prunus dulcis) as a low cost adsorbent, J. Chem. Eng. Data 56 (2011) 2136–2147.
[79] F. Arias Arias, M. Guevara, T. Tene, P. Angamarca, R. Molina, A. Valarezo, O. Salguero, C. Vacacela Gomez, M. Arias, L.S. Caputi, The adsorption of methylene blue on eco-friendly reduced graphene oxide, Nanomaterials 10 (2020) 681.
[80] K.J. Laidler, The dev elopment of the Arrhenius equation, J. Chem. Educ. 61 (1984) 494–498.
[81] M. Mralik, Adsorption, chemisorption, and catalysis, Chem. Pap. 68 (2014) 1625–1638.
[82] H. Freundlich, Adsorption solution, J. Phys. Chem. 57 (1906) 384–470.
[83] M.I. Temkin, V. Pyzhev, Kinetics of ammonia synthesis on promoted iron catalyst, Acta Phys. Chim. USSR 12 (1940) 327–356.
[84] Q. Hu, Z. Zhang, Application of Dubinin–Radushkevich isotherm model at the solid/solution interface: a theoretical analysis, J. Mol. Liq. 277 (2019) 646–648.
[85] I. Langmuir, Adsorption of gases on plain surfaces of glass mica platinum, J. Am. Chem. Soc. 40 (1918) 1361–1403.
[86] X. Xing, H. Qu, R. Shao, Q. Wang, H. Xie, Mechanism and kinetics of dye desorption from dye-loaded carbon (XC-72) with alcohol-water system as desorbent, Water Sci. Technol. 76 (2017) 1243–1250.
[87] X. Xing, H. Qu, P. Chen, B. Chi, H. Xie, Studies on competitive adsorption of dyes onto carbon (XC-72) and regeneration of adsorbent, Water Sci. Technol. 74 (2016) 2505–2514.
[88] J. Yang, S. Shojaei, S. Shojaei, Removal of drug and dye from aqueous solutions by graphene oxide: adsorption studies and chemometrics methods, NPJ Clean Water 5 (2022) 5.